HZDR-125

FRACTURE MECHANICS INVESTIGATION OF REACTOR PRESSURE VESSEL STEELS BY MEANS OF SUB-SIZED SPECIMENS (KLEINPROBEN)

REACTOR SAFETY RESEARCH – PROJECT NO.: 1501592B FINAL REPORT

A. Das, E. Altstadt, P. Chekhonin, M. Houska

Wissenschaftlich-Technische Berichte
HZDR-125 · 2022 · ISSN 2191-8708

WISSENSCHAFTLICH-
TECHNISCHE BERICHTE

HZDR
HELMHOLTZ ZENTRUM
DRESDEN ROSSENDORF

Wissenschaftlich-Technische Berichte
HZDR-125

A. Das, E. Altstadt, P. Chekhonin, M. Houska

FRACTURE MECHANICS INVESTIGATION OF REACTOR PRESSURE VESSEL STEELS BY MEANS OF SUB-SIZED SPECIMENS (KLEINPROBEN)

REACTOR SAFETY RESEARCH – PROJECT NO.: 1501592B FINAL REPORT

HZDR
HELMHOLTZ ZENTRUM
DRESDEN ROSSENDORF

Druckausgabe: ISSN 2191-8708

Elektronische Ausgabe: ISSN 2191-8716

https://www.hzdr.de/publications/Publ-36701

urn:nbn:de:bsz:d120-qucosa2-843791

2023

Herausgegeben vom

Helmholtz-Zentrum Dresden - Rossendorf

Bautzner Landstraße 400

01328 Dresden

Germany

Abschlussbericht

Final Report

Reaktorsicherheitsforschung – Vorhaben-Nr.: 1501592B

Reactor Safety Research – Project No.: 1501592B

Vorhabenstitel: Bruchmechanische Untersuchung von Reaktordruckbehälterstählen mittels Kleinprobentechnik

Project title: Fracture mechanics investigation of reactor pressure vessel steels by means of sub-sized specimens

Acronym: KLEINPROBEN

Autoren / Authors: A. Das, E. Altstadt, P. Chekhonin, M. Houska

Dienststelle des Autors / Performing Organization: TU Dresden, Lehrstuhl für Radiochemie in Kooperation mit dem Helmholtz-Zentrum Dresden-Rossendorf e.V.

Berichtsdatum / Publication Date: 31.03.2023

Berichts – Nr. / Report – No:
(Nur wenn eine von ZE/AN vergeben wird.)

Das diesem Bericht zugrunde liegende Vorhaben wurde mit Mitteln des Bundesministeriums für Umwelt, Naturschutz, nukleare Sicherheit und Verbraucherschutz (BMUV) unter dem Förderkennzeichen 1501592B gefördert

Bundesministerium
für Umwelt, Naturschutz, nukleare Sicherheit
und Verbraucherschutz

Table of Contents

Kurzfassung

Die Versprödung von Reaktordruckbehälter (RDB)-Stählen durch Neutronenbestrahlung schränkt die Betriebsdauer von Kernreaktoren ein. Die Referenztemperatur T_0, die aus bruchmechanischen Prüfungen unter Verwendung des Master Curve-Konzepts ermittelt wird, ist ein guter Indikator für die Bestrahlungsbeständigkeit eines Werkstoffs. Die Messung der Verschiebung von T_0 nach Neutronenbestrahlung unter Verwendung des Master Curve-Konzepts, die mit der Versprödung des Materials einhergeht, ermöglicht die Bewertung der Reaktorwerkstoffe. Im Kontext der weltweit realisierten Laufzeitverlängerung von Kernkraftwerken wird das Fehlen von ausreichenden Mengen von mitbestrahlten Materialproben zur Herausforderung. Die Prüfung von kleinen 0,16T C(T)-Proben, die aus bereits geprüften Charpy-Standardproben hergestellt wurden, hilft, das Problem der Materialknappheit zu lösen.

Vier RRDB-Stähle mit unterschiedlichen Zusammensetzungen wurden im unbestrahlten und im neutronenbestrahlten Zustand untersucht. Insgesamt wurden 189 Mini-CT-Proben hergestellt und geprüft. Ein Aspekt dieser Studie war die Übertragbarkeit der mit Mini-C(T)-Proben ermittelten bruchmechanischen Daten. Die Ergebnisse zeigen, dass die mit Mini-C(T) ermittelten Referenztemperaturen gut mit denen von Charpy-Standardproben übereinstimmen. RDB-Stähle mit höheren Cu- und P-Gehalten weisen einen höheren bestrahlungsinduzierten Anstieg von T_0 auf. Die Bruchflächen wurden mittels REM untersucht, um die Lage der Bruchinitiatoren zu erfassen. Auch die Bruchmoden wurden bestimmt. Eine große Anzahl von Prüfergebnissen (durch Hinzunahme von weiteren, außerhalb des Vorhabens generierten Versuchsdaten) bildete die Grundlage für eine Zensierungs-Wahrscheinlichkeitsfunktion in Abhängigkeit der Prüftemperatur, die zur optimalen Auswahl der Prüftemperatur bei der Master-Curve-Prüfung verwendet wurde. Die Auswirkung des Zensierungskriteriums für langsames stabiles Risswachstum aus ASTM E1921 auf die Bestimmung von T_0 wurde analysiert und es wurde festgestellt, dass sie nur einen geringen Einfluss hat. Die Ergebnisse belegen die Gültigkeit der Mini-C(T)-Probenprüfung und bestätigen die Rolle der Verunreinigungselemente Cu und P bei der Neutronenversprödung. Für weiterführende Forschungsarbeiten wird empfohlen, die Mikrostruktur mit den Brucheigenschaften von Werkstoffen vor und nach der Neutronenbestrahlung zu verknüpfen, sowie die Master-Curve-Prüfung unter Verwendung der Ergebnisse unserer statistischen Analyse zu optimieren.

Abstract

The embrittlement of reactor pressure vessel (RPV) steels due to neutron irradiation restricts the operating lifetime of nuclear reactors. The reference temperature T_0, obtained from fracture mechanics testing using the Master Curve concept, is a good indicator of the irradiation resistance of a material. The measurement of the shift in T_0 after neutron irradiation, which accompanies the embrittlement of the material, using the Master Curve concept, enables the assessment of the reactor materials. In the context of worldwide life time extensions of nuclear power plants, the limited availability of neutron irradiated materials (surveillance materials) is a challenge. Testing of miniaturized 0.16T C(T) specimens manufactured from already tested standard Charpy-sized specimens helps to solve the material shortage problem.

In this work, four different reactor pressure vessel steels with different compositions were investigated in the unirradiated and in the neutron-irradiated condition. A total number of 189 mini-C(T) samples were fabricated and tested. An important component of this study is the transferability of fracture mechanics data from mini-C(T) to standard Charpy-sized specimen. Our results demonstrate good agreement of the reference temperatures from the mini-C(T) specimens with those from standard Charpy-sized specimens. RPV steels containing higher Cu and P contents exhibit a higher increase in T_0 after irradiation. The fracture surfaces were investigated using SEM in order to record the location of the fracture initiators. The fracture modes were also determined.

A large number of test results formed the basis for a censoring probability function, which was used to optimally select the testing temperature in Master Curve testing. The effect of the slow stable crack growth censoring criteria from ASTM E1921 on the determination of T_0 was analysed and found to have a minor effect. Our results demonstrate the validity of mini-C(T) specimen testing and confirm the role of the impurity elements Cu and P in neutron embrittlement. We anticipate further research linking microstructure to the fracture properties of materials before and after neutron irradiation and the optimization of Master Curve testing using the results from our statistical analysis.

1 Introduction

In RPV steels containing Cu and P, neutron irradiation induces embrittlement due to the formation of Cu-rich, nm-sized, clusters and P segregations at grain boundaries. In low-Cu and low-P steels, irradiation induced Mn-Ni-Si rich clusters are the dominating features for embrittlement. The embrittlement caused by Cu clusters and Mn-Ni-Si clusters is associated with radiation hardening, i.e. an increase of flow stress through dislocation pinning. In contrast, P segregations at grain boundaries cause a so-called non-hardening embrittlement [1,2]. Such effects can lead to an increase in T_0, the reference temperature, which is determined using fracture toughness testing with the Master Curve concept. The Master Curve concept correlates the median fracture toughness of a material to the test temperature in the ductile to brittle regime. A three-parameter Weibull distribution considers the inherent scatter in fracture toughness values and the specimen size effect in the Master Curve concept.

In order to ensure continued safe operation of European reactors, it is necessary to solve specific issues that arise from irradiation induced reactor pressure vessel embrittlement under long-term operation. The shift in the reference temperature T_0 of a material, which is a consequence of neutron embrittlement, can be determined using fracture mechanics testing in combination with the Master Curve concept. The limited availability of surveillance materials poses a challenge for the feasibility of such testing. The use of mini-C(T) specimen technology is a promising option to overcome the lack of materials. For example, 8 mini-C(T) specimens (0.16T C(T), 4 mm thickness) can be manufactured from one tested standard Charpy sized specimen (10 × 10 × 55 mm), allowing a reliable determination of the reference temperature T_0.

2 Objectives and scope of the project

The objectives of this study are:

1. To establish a procedure for fracture mechanics testing of neutron-irradiated RPV steels using mini-C(T) specimens with respect to manufacturing of specimens, precracking, and measurement of the crack opening displacement / load line displacement
2. Investigation of material specific fracture mechanics properties as a function of irradiation conditions

3. To demonstrate the transferability of fracture mechanics data from mini-C(T) to standard Charpy-sized specimens
4. Investigation of fracture surfaces in order to determine location of fracture initiation sites and determination of fracture modes

Additional objectives achieved outside of the scope of the project:

5. To optimize the Master Curve testing procedure with respect to the selection of the testing temperature using a censoring probability function based on a large number of tests
6. To study the impact of the stable crack growth censoring criterion ($K_{\mathrm{Jc}\Delta\mathrm{a}}$) on the determination of T_0

The investigations were part of the joint sub-projects 1501592A, carried out by Framatome, and 1501592B, carried out by TU Dresden/HZDR. This report is related to the work performed by TU Dresden/HZDR.

The joint work was organized in seven work packages:

- WP0: Management and coordination (performed by Framatome)
- WP1: Fabrication of mini-C(T) samples; It includes the manufacture of sub-sized 0.16 C(T) specimens from the HZDR and Framatome stock. The manufacturing of specimens from irradiated materials is carried out in the hot cells of HZDR.
- WP2: Determination of the reference temperatures T0 according to the Master curve procedure; The samples are tested according to the Master Curve concept to determine T_0 both in the unirradiated and irradiated states (WP2).
- WP3: Fractography; is performed on the broken samples using scanning electron microscopy (SEM)
- WP4: Detailed comparison between mini-C(T) and standard Charpy-sized specimens is performed
- WP5: Numerical simulations by finite elements analysis (FEM), solely performed by Framatome (not included in this report)
- WP6: Documentation; includes the final reports for both sub-projects

A close interaction of the KLEINPROBEN joint project was established with related Euratom projects FRACTESUS and ENTENTE. This included mutual information on results and exchange of experimental data.

3 Literature review

In the Master Curve concept, which correlates the median fracture toughness and the test temperature in the ductile to brittle regime, a three-parameter Weibull distribution takes into account the inherent scatter in fracture toughness values [3] and the specimen size effect [4]. The shape of the Master Curve tends to stay the same after neutron irradiation on various RPV steels [5], therefore, justifying the use of this concept. Availability of neutron-irradiated material is a well-known problem associated with Master Curve testing. Besides solving the material availability limitation [4], the miniaturization of test specimens also reduces the active sample volume.

It was found that the T_0 obtained from 1T C(T) specimens [6–8] was larger than the one obtained from the Charpy-sized three-point (single edge) bend specimens (SE(B)) of 10 × 10 × 55 mm dimension [6,7,9,10]. A better compatibility of 1T C(T) was found with 1T SE(B) in [7]. To solve the shortage of irradiated materials, the use reconstituted and sub-sized specimens techniques [11,12] proved to be beneficial. The T_0 values and the location of the fracture initiators from mini-C(T) specimens with 4 mm thickness [13–19] were reported to be similar to the ones found for larger C(T) specimens. Some reported similar T_0 values [20] for mini-C(T) and 0.5T C(T) specimens while a difference of 12-14 K was reported between mini-C(T) and large C(T) specimens by others [8,21]. Chaouadi et al. reported a bias of ±10 K between standard Charpy-sized and mini-C(T) specimens [8]. Since no clear conclusion is reached thus far, the comparison of T_0 obtained from mini-C(T) and standard Charpy-sized specimens needs further validation. Therefore, we tested 0.16T mini-C(T) specimens manufactured from already tested SE(B) standard Charpy-sized specimens using the Master Curve concept and obtained the reference temperature T_0 for four different RPV steels (in unirradiated and irradiated states). We then compared the reference temperatures of the mini-C(T) specimens with the standard Charpy-sized specimens.

Neutron irradiation induces neutron embrittlement due to the formation of Cu-rich [1,22] clusters and P segregations [1,23] in RPV steels containing Cu and P, respectively. This can lead to an increase in T_0 [24]. In this study, we investigated the effect of chemical composition on neutron irradiation by selecting four western RPV steels with varying chemical compositions.

Wallin et al. [19,25] observed no significant differences between the locations of the fracture initiators in mini-C(T) and larger C(T) and SE(B) specimens. They also found that side grooving had a clear but not a dramatic effect on the location of the fracture initiators. Previous works found higher fracture toughness for RPV steel samples, where fracture initiators were located away from crack front [10,26]. Tanguy et al. [27] also observed similar results for Charpy Impact specimens. They also found that in samples with large ductile regions, the fracture initiators were located close to the centre of the specimen. An essential part of this research is devoted to the location analysis of fracture initiators. Fracture modes are also determined using SEM and correlated with the net hardening effect.

The optimum selection of the next test temperature in Master Curve testing is not straight forward, especially for smaller sample pools (for example in neutron-irradiated specimens) as the validity criterion of ASTM E1921 $\sum r_i \cdot n_i \geq 1$ may not be fulfilled (where r is the number of uncensored valid data and n is the specimen weighting factor, which depends on the $T - T_0$ value). Testing at temperatures close to T_0 may lead to censoring due to the fracture toughness K_{Jc} exceeding the K_{Jclimit} and/or violating the $K_{\mathrm{Jc\Delta a}}$ criteria (slow stable crack growth before cleavage) of ASTM E1921-21 [28]. Testing at too low temperatures ($T - T_0$ < - 50 K) also leads to test results being invalid. It was reported in [13] that a $T - T_0$ value below -30 K prevented the censoring of tests. To optimize the determination of the next test temperature, two competing aspects must be taken into account:

- Testing at comparatively high temperatures close to T_0 to improve the quality of the fit (and obtain the highest weighting factor n)
- Avoiding censoring: this speaks for testing at comparatively low temperatures but not below $T - T_0 = -50\ \mathrm{K}$

The censoring criteria K_{Jclimit} and $K_{\mathrm{Jc\Delta a}}$ can affect the T_0. While the K_{Jclimit} censoring criterion can be checked easily during the Master Curve analysis, the $K_{\mathrm{Jc\Delta a}}$ censoring criterion requires an additional optical or scanning electron microscope (SEM) investigation of the fracture surface. With the help of a large number of Master Curve testing results and fractography, we check the effect of the violation of the $K_{\mathrm{Jc\Delta a}}$ criterion (section 8.9.2 and 10.2.1 of ASTM E1921-21) on the determination of T_0.

4 Experiments

4.1 Materials

Four RPV steels were investigated in this project, three base and one weld metal. Amongst the base metals, we investigated A533B Cl.1 (referred here as 3JRQ57 or JRQ), A508 Cl.3 (referred here as 1JFL11 or JFL) and 22NiMoCr3-7 (referred here as ANP-3). The manufacturing of JRQ, the European reference material 3JRQ57, involved casting and rolling followed by heat-treatment that included austenization at 900 °C with oil quenching, tempering at 665 °C for 12 hours and stress release annealing at 620 °C for 40 hours. A detailed account of the material can be found in [29]. Kawasaki Steel Corporation manufactured JFL through casting, forging and heat-treatment, which included austenization at 880 °C with oil quenching followed by tempering at 640 °C for 9 hours with air-cooling. The chemical composition of JFL was similar to JRQ except that it contained lower amounts of Cu and P as compared to JRQ. ANP-3, provided to HZDR by Framatome and manufactured by Klöckner, contained lower Mn but higher Ni and Mo contents as compared to JRQ and JFL. It was manufactured by forging followed by heat treatment and tempering. The weld metal S3NiMo1 (referred here as ANP-6) was provided to HZDR from Framatome and contained low C and high Ni content. The composition of the four RPV steels can be found in Table 1 along with the compositions of other RPV steels chosen for censoring statistics (described below).

Going beyond the scope of the project, we utilize the test results from the four RPV steels used in this study together with test results from other RPV steels to develop censoring statistics of mini-CT specimens. The database includes a total number of 381 mini-CT tests from 11 different materials. The chemical compositions are listed in Table 1. Table 2 contains the mechanical properties (yield strength at room temperature (RT), Charpy impact transition temperature at 41J and the upper shelf energy from Charpy impact tests) along with the total number N of valid tests carried out (uncensored + censored data). A combination of base and weld metals both in their unirradiated (300 samples) and irradiated states (81 samples) are included in the statistics. With a few exceptions, most of the materials also contributed to the verification of the $K_{\mathrm{Jc}\Delta\mathrm{a}}$ censoring criterion. For this, the measurement of the ductile crack growth region was performed according to ASTM E1921 using either an optical or a scanning

electron microscope. The use of SEM was found to be more suitable for ductile crack growths that were close to the limit of $K_{\mathrm{Jc\Delta a}}$ censoring criterion.

Table 1 Composition of all materials included in this study

Common name	Material	C	Si	Mn	Cr	Ni	Mo	Cu	P	V
Base Metals										
3JRQ57/ 5JRQ56B1	A533B Cl.1 [29]	0.18	0.24	1.42	0.12	0.84	0.51	0.14	0.017	0.002
1JFL11	A508 Cl.3 [30]	0.17	0.25	1.42	0.16	0.75	0.52	0.01	0.002	0.004
ANP-3	22Ni-MoCr3-7 [31]	0.23	0.20	0.70	0.44	0.98	0.79	0.12	0.015	-
Biblis-C	22Ni-MoCr3-7 [32]	0.21	0.2	0.90	0.41	0.87	0.53	0.04	0.008	0.007
GW8-BM / FZD-4	15Kh2MFAA [33]	0.15	0.30	0.45	2.86	0.10	0.79	0.05	0.008	0.31
CRIEPI	SQV2A [18]	0.22	0.25	1.46	0.11	0.69	0.57	-	0.002	-
Weld Metals										
ANP-6	S3NiMo1 [31]	0.05	0.15	1.41	0.07	1.69	0.46	0.08	0.012	0.004
ANP-2	S3NiMo1 [33]	0.06	0.08	1.05	0.04	1.02	0.63	0.03	0.017	<0.01
ANP-5	NiCrMo1 [34]	0.08	0.15	1.10	0.74	1.11	0.60	0.22	0.015	0.001

Table 2 Materials included in censoring statistics with their irradiation state, mechanical properties, total number of specimens tested (N) and whether they are included in the verification of the $K_{\mathrm{Jc\Delta a}}$ censoring criterion

Common name	Material	Condition	Yield Strength at RT (MPa)	T41J Charpy (°C)	Upper shelf energy (J)	N	$K_{\mathrm{Jc\Delta a}}$
3JRQ57	A533B Cl.1	Unirradiated[9,30]	484	–13.2	192.3	28	Yes
		Irradiated[9,30]	843	208.5	111.4	14	Yes
5JRQ56B1		Unirradiated	484	–13.2	192.3	25	No
CRIEPI	SQV2A (A533B Cl.1)	Unirradiated[18]	477	-90	-	39	Yes
1JFL11	A508 Cl.3	Unirradiated[30]	470	–42.6	211.2	41	Yes
		Irradiated[9,30]	640	35.7	195.5	36	Yes
ANP-3	22NiMoCr3-7	Unirradiated[6,34,35]	423	–50	194	16	Yes
		Irradiated[34]	597	-	-	16	Yes
Biblis-C		Unirradiated[36]	444	–42	186	17	No
GW8-BM	15Kh2MFAA	Unirradiated	534	-	-	20	No
FZD-4		Unirradiated[33]	532	–55	191	34	Yes
ANP-6	S3NiMo1	Unirradiated[34,37]	555	–55	174	31	Yes
		Irradiated[34,37]	817	123	-	15	Yes
ANP-2		Unirradiated[34,37]	516	–7	197	18	Yes
ANP-5	NiCrMo1	Unirradiated[34,37]	604	–12	145	31	Yes

4.2 Irradiation experiments

Samples of JFL and JRQ were neutron-irradiated in the WWER-2 reactors in Rheinsberg up to a fluence of 10^{20} n/cm^2 at 255 °C [9]. This fluence correspond to approximately ten times the German end-of-life (EOL) criterion, which limits the maximum neutron fluence in RPV walls of pressurised water reactors to 10^{19} n/cm² (E > 1 MeV) [38]. Samples of ANP-3 and ANP-6 were neutron-irradiated at the VAK Kahl nuclear reactor at lower neutron fluences as compared to JRQ and JFL. Table 3 lists the irradiation details.

Table 3 Neutron irradiation conditions for tested specimens

Common name	Material	Fluence 10^{19} n/cm^2 E > 1MeV	Max flux 10^{12} n/cm^2/s E > 1MeV	Irradiation Temperature °C	Irradiation time Days
3JRQ57	A533B Cl.1	9.82	5.37	255	297
1JFL11	A508 Cl.3	8.67	4.74	255	297
ANP-3	22NiMoCr3-7	3.9	1.83	285	
ANP-6	S3NiMo1	5.6	2.51	277-286	

4.3 Master Curve testing

Master Curve testing of the four RPV steels was performed on unirradiated and neutron irradiated 0.16T mini-C(T) specimens. The number of samples tested for each state can be found in Table 2. Typically, eight 0.16T C(T) samples were extracted from one standard Charpy-sized SE(B) specimen, four from each half as shown in Fig. 1 which shows an example of a L-T oriented SE(B) specimen half used to manufacture four L-T oriented 0.16T C(T) specimens. The determination of reference temperature T_0 was performed using the multi-temperature method according to ASTM E1921-21 [28]. The 0.16T C(T) specimens were fatigue pre-cracked and 20% side grooved in the unirradiated state. No side-grooves were used in the irradiated state. It is important to emphasize that side grooving neither significantly affected the determination of T_0 [8,20] nor the location of the fracture initiation [19].

The specimens were monotonically loaded with a test speed of 0.1 mm/min. Quasi-static testing was performed using the Inspekt10 machine (10 kN maximum force) for the unirradiated specimens and using the MTS 50 machine (50 kN maximum force) fitted with a 10 kN load cell, to increase precision, for the irradiated specimen. The irradiated specimens were tested in the hot cells of Helmholtz-Zentrum Dresden-Rossendorf (HZDR). Sandner clip-on gauges were used on the front face to measure the front face displacements (FFD) which were converted to load-line displacements (LLD) using the conversion method as stated by Landes [39] with a rotation factor of $r = 0.352$.

A preliminary T_0 for the 0.16T C(T) specimen was assumed to be 20 K lower than the reference temperature determined for pre-cracked standard Charpy-sized specimens using the Master Curve concept [18]. Guided by the statistically based concept for optimum test temperature selection (discussed later), the tests were performed at temperatures below the reference temperature until failure (most often by cleavage fracture). The initial crack lengths were measured at nine equally spaced points as required in ASTM E1921-21 using optical microscopy. The recorded load-displacement values were used to calculate the K_{Jc} values for the individual tests, which were thereafter used to plot the master curves. To check the violation of the $K_{\mathrm{Jc\Delta a}}$ censoring criterion, an additional optical or scanning electron microscope investigation of the fracture surface was undertaken and the slow stable crack growth at the longest crack dimension was measured as mentioned in ASTM E1921-21.

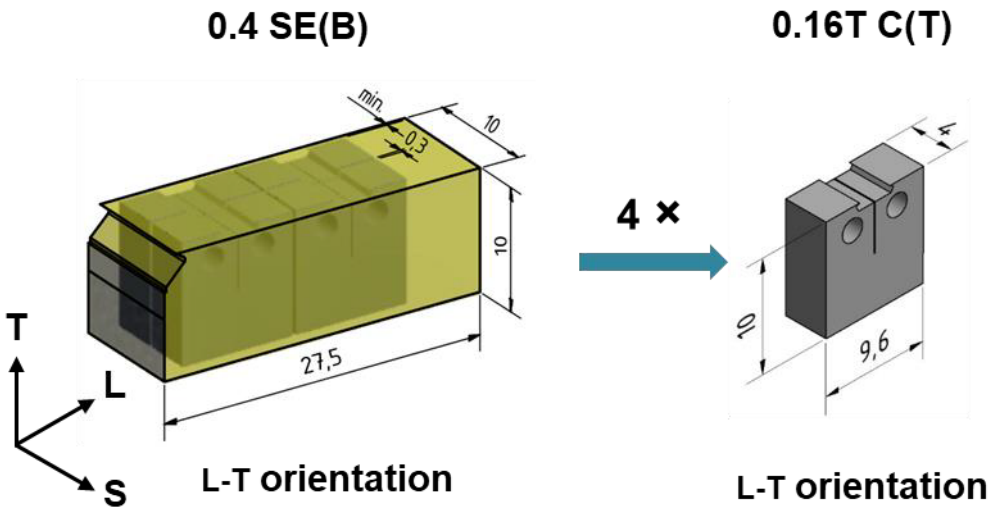

Fig. 1 Cutting scheme of 0.16T C(T) specimens manufactured from a standard Charpy-sized SE(B) specimen

4.4 Fractography

4.4.1 Identification of primary fracture initiation site

Scanning electron microscope was used to investigate the fracture surfaces with respect to the location of the primary fracture initiation site. The distances to the crack front as well as the side surface was measured as soon as the primary fracture initiation site was located. As most of the samples failed by cleavage or transgranular fracture, the fracture initiation site was located by tracing back the river lines or cleavage facets to their point of origin. Along with the primary fracture initiation site, samples often exhibited secondary fracture initiation sites. These were however, arrested locally. The fractography of secondary fracture sites is beyond the scope of this project. To distinguish between primary and secondary initiation sites, a low magnification overview SEM image was used as shown in Fig. 2. Through visual inspection, the major river lines were traced back to the primary site, which were often located close to the centre of the sample and dominated the fracture surface. The secondary flow lines on the other hand, were often located close to the edges and occupied a small fraction of the fracture surface.

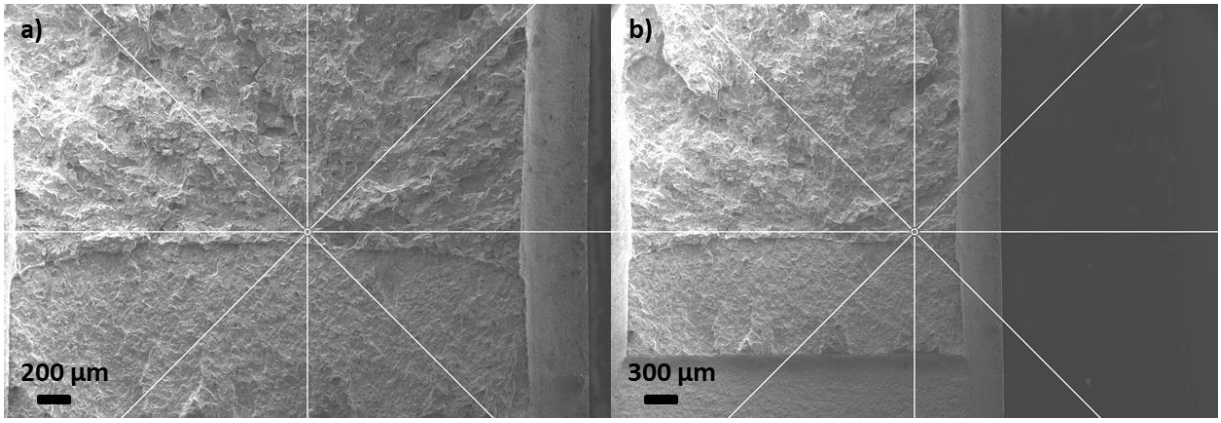

Fig. 2 SEM overview images of the fracture surfaces indicating the a) primary and the b) secondary fracture initiation site. This example is taken from an unirradiated JRQ sample in the TL orientation tested at -105 °C.

To precisely locate the primary fracture initiation site, three line images at medium magnification were obtained as shown in Fig. 3 and Fig. 4 for both the broken samples sides using the secondary electron (SE) mode, a working distance of 17 mm and a probe current of 1000 pA. The aperture size used was 50 µm along with a voltage of 15 kV. Once the area containing the primary initiation site is identified, higher resolution images are needed to determine the exact location of the fracture initiator. To this end, SE images at higher magnifications were taken with a lower working distance of 7 mm and a lower probe current of 500 pA as shown in Fig. 5. The exact distance of the fracture initiator to the crack front was measured using these images while distance to the side surface was measured using the overview image in Fig. 2a.

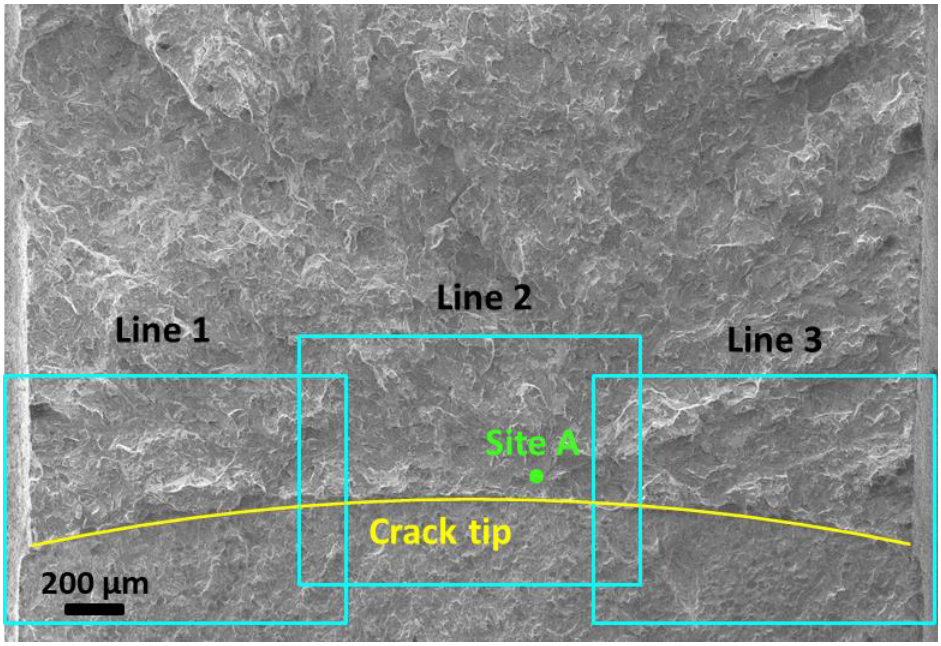

Fig. 3 Fracture surface secondary electron image of a broken sample. The crack tip is formed by fatigue pre-cracking. Line images 1-3 are taken at medium resolution in order to locate the primary fracture initiation site. Site A signifies the location of the primary fracture.

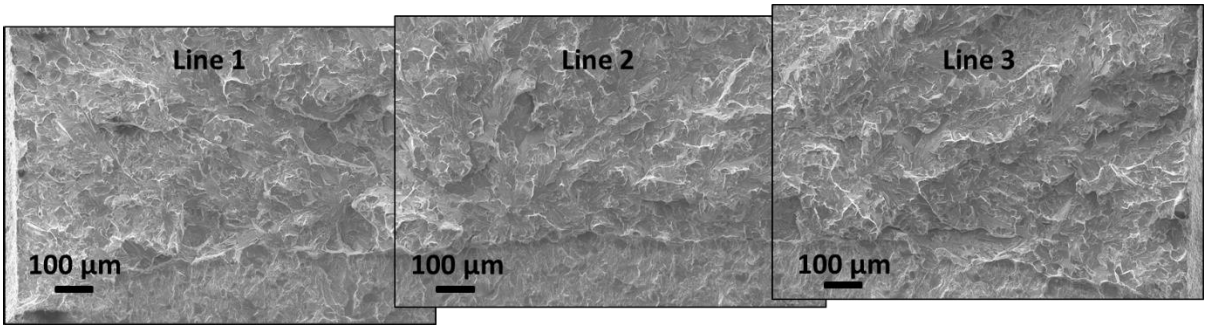

Fig. 4 Three line images with overlapping edges covering the fracture area close to the crack tip. This example is taken from an unirradiated JRQ sample in the TL orientation tested at -105 °C.

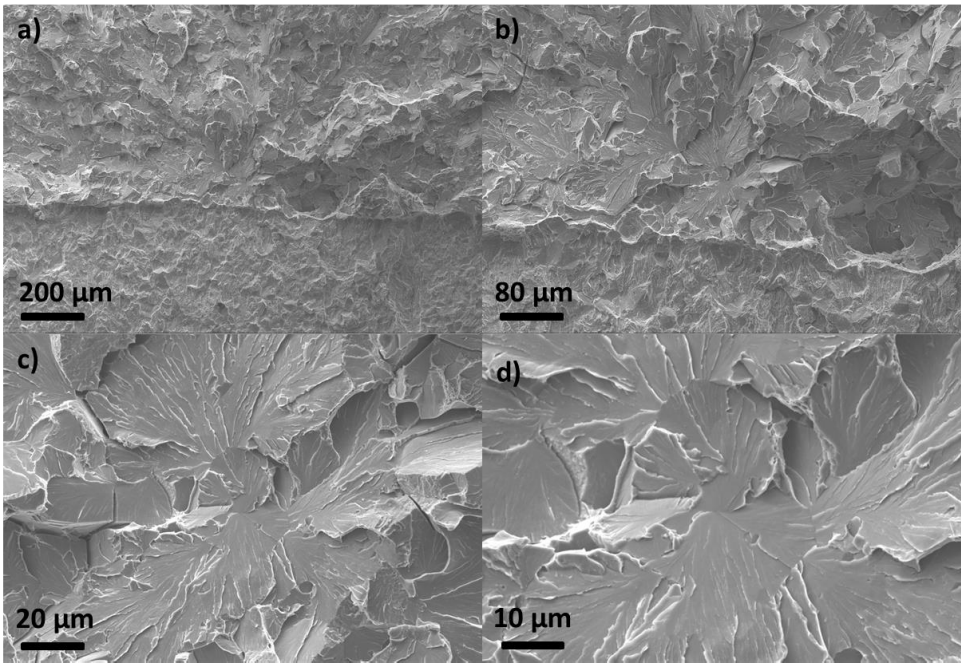

Fig. 5 SEM SE images of the primary fracture initiation site at progressively higher magnifications. This example is taken from an unirradiated JRQ sample in the TL orientation tested at -105 °C.

4.4.2 Ductile crack growth

Stable ductile crack growth before cleavage fracture may lead to the violation of the $K_{\mathrm{Jc\Delta a}}$ censoring criterion according to ASTM E1921. To check this, the measurement of the ductile crack growth region was performed according to ASTM E1921 using either an optical or a scanning electron microscope. The use of SEM was found to be more suitable for ductile crack growths that were close to the limit of $K_{\mathrm{Jc\Delta a}}$ censoring criterion as shown in Fig. 6. Here regions 1 and 2 depict ductile and cleavage fracture, respectively.

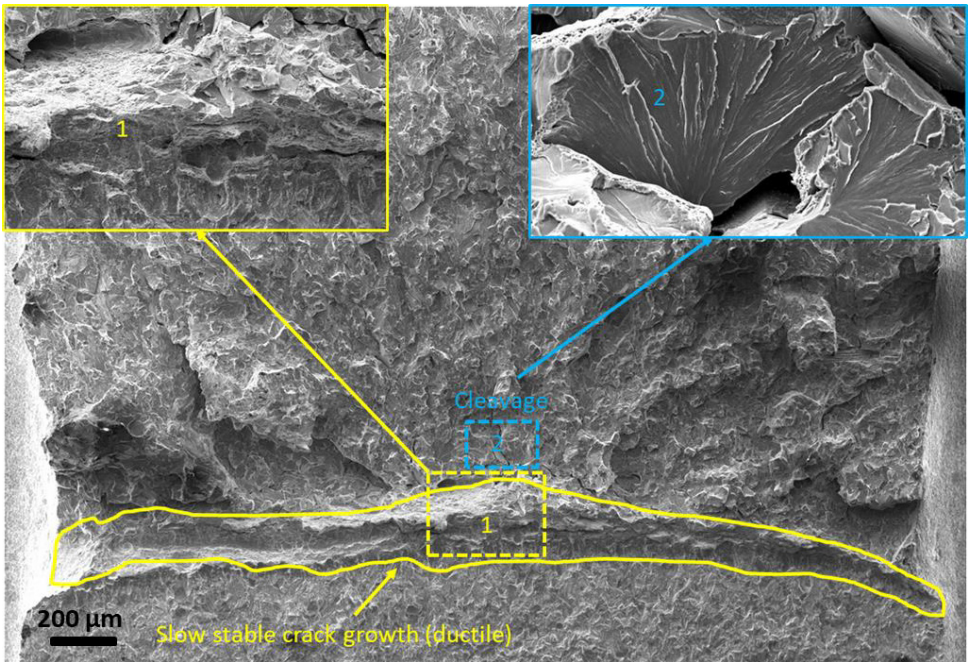

Fig. 6 SE image of a fractured surface with a stable ductile crack growth region (1) close to the crack tip. The cleavage fracture follows the ductile region as indicated in (2).

4.4.3 Fracture mode

An equally spaced grid with 100 µm spacing is masked over the fracture surface of a line image as shown in Fig. 7 for an irradiated sample of JRQ in the T-L orientation with a $T - T_0$ of -19.5 K. This is done to record the relative fractions of ductile, intergranular (IG) and cleavage fracture modes on the fracture surfaces of unirradiated as well as the irradiated samples. For each grid circle, the fracture mode at its centre is recorded. This is repeated for all the line images of one side of a fractured sample to approximately obtain 200 grid circles. In Fig. 7, the ductile regions are marked with yellow, IG with black and cleavage with white grid circles. A high-resolution image from the same fracture surface is shown in Fig. 8, which reveals ductile, IG and cleavage fracture modes that are marked with yellow, black and white arrows, respectively.

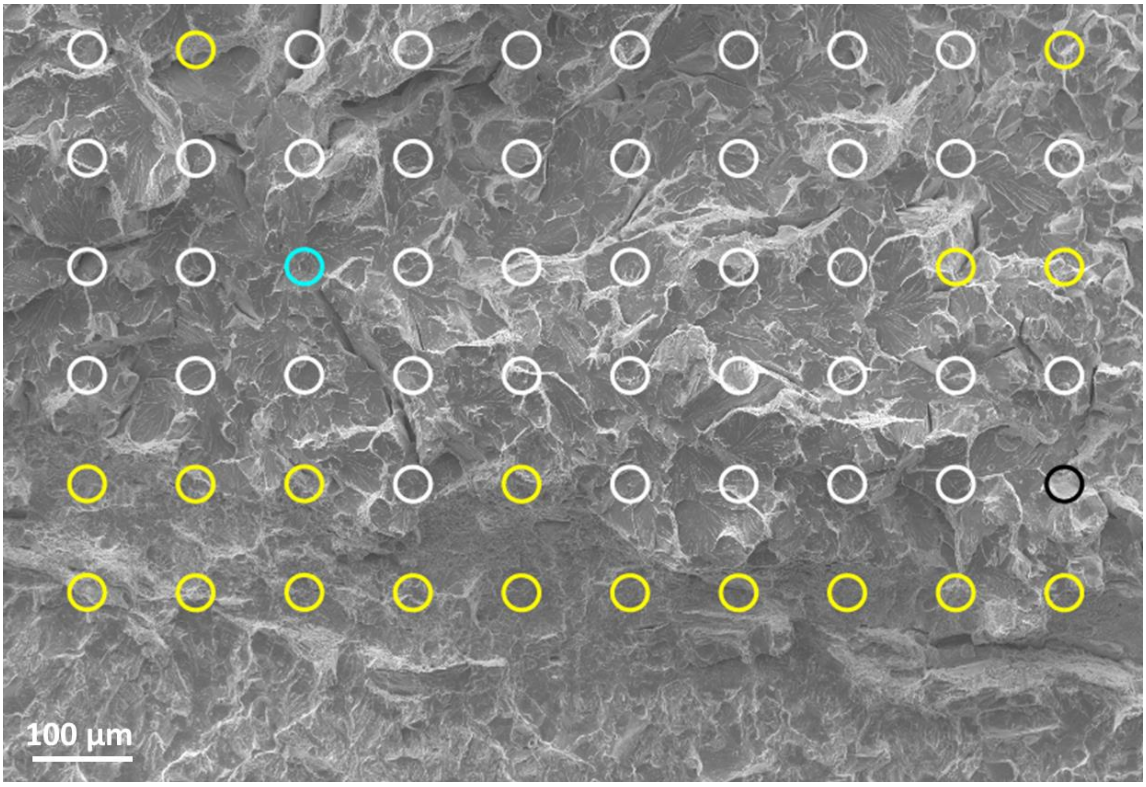

Fig. 7 An equi-spaced grid masked over a line image of a fractured side of an irradiated JRQ sample in the T-L orientation. Ductile, IG and cleavage fracture modes are marked by yellow, black and white grid circles, respectively.

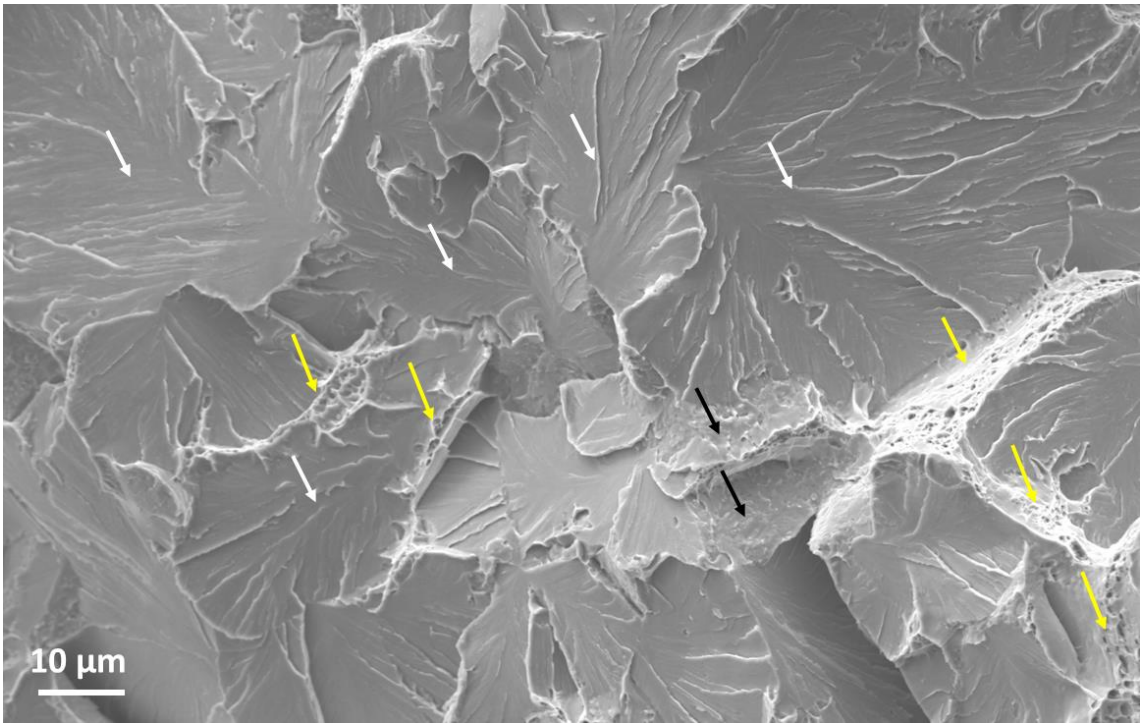

Fig. 8 High-resolution SE image of the fracture surface of an irradiated JRQ sample showing ductile, IG and cleavage fracture modes and are marked with yellow, black and white arrows, respectively.

5 Results

5.1 Master Curve testing

Master Curve tests performed on the RPV steels yielded the reference temperatures for both the unirradiated and irradiated states. Fig. 9 to Fig. 13 plots the individual K_{Jc} values, converted to $K_{\mathrm{Jc(1T)}}$ equivalent values (as open circles), against the testing temperature. The K_{Jc} median (dashed line) along with the 98% and 2% tolerance bound curves are also plotted. The $K_{\mathrm{Jc(1T)}}$ values marked as crosses are invalid values either due to failing the $T - T_0$ > -50 °C invalidation criterion or due to an invalid crack shape [27]. The values marked as triangles are fracture toughness values which exceed the K_{Jclimit} censoring criterion and/or the $K_{\mathrm{Jc\Delta a}}$. These values are censored during the determination of T_0 i.e. they are replaced either by the K_{Jclimit} value or the highest uncensored K_{Jc} value depending on which criterion is violated. The reference temperature T_0, defined as the temperature when K_{Jc} median reaches a value of 100 MPa√m, is determined using ASTM E1921-21.

Dotted validity window is marked with the temperature limits of $T_0 \pm 50\ K$ and K_{Jclimit} values calculated using the lowest ligament length of the test series. The individual K_{Jclimit} values in the Master Curve analysis on the other hand were calculated using varying ligament lengths. Therefore, in some instances (like in Fig. 9 JRQ irradiated), a valid data point may appear outside the validity window, but in reality, it is not. The reference temperature (T_0) and the shift in reference temperature (ΔT_0) along with the number of valid uncensored tests (r), total number of valid tests (N), the value of $\sum r_i \cdot n_i$ and the standard deviation (σ) from both the unirradiated to the irradiated states are listed in Table 4. The highest value of $\sum r_i \cdot n_i$ was obtained for the testing of unirradiated JFL in the T-S orientation and lowest was obtained for unirradiated ANP-6 in the T-L orientation. Testing in different orientations T-L, T-S and L-T resulted in T_0 values that agreed within the error margins (standard deviations) of the test series.

An increase in the reference temperature was observed for all materials from unirradiated to the irradiated state, more for JRQ and ANP-6 as compared to JFL and ANP-3 (Fig. 14 and Table 4). For the JFL material, a change in the orientation resulted in only a small difference in the shift in reference temperature (ΔT_0), see also [40].

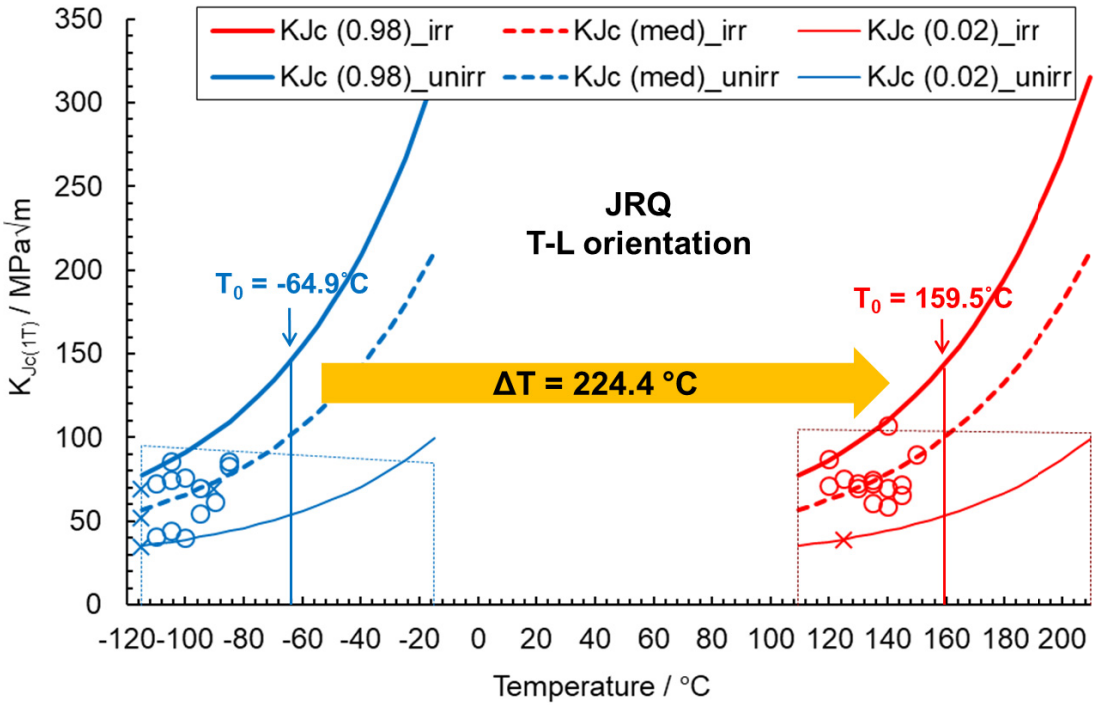

Fig. 9 $K_{\mathrm{Jc(1T)}}$ versus temperature with K_{Jc} median (dashed) along with 98% and 2% tolerance bounds for JRQ T-L orientation in the unirradiated and the irradiated states showing the shift in reference temperature

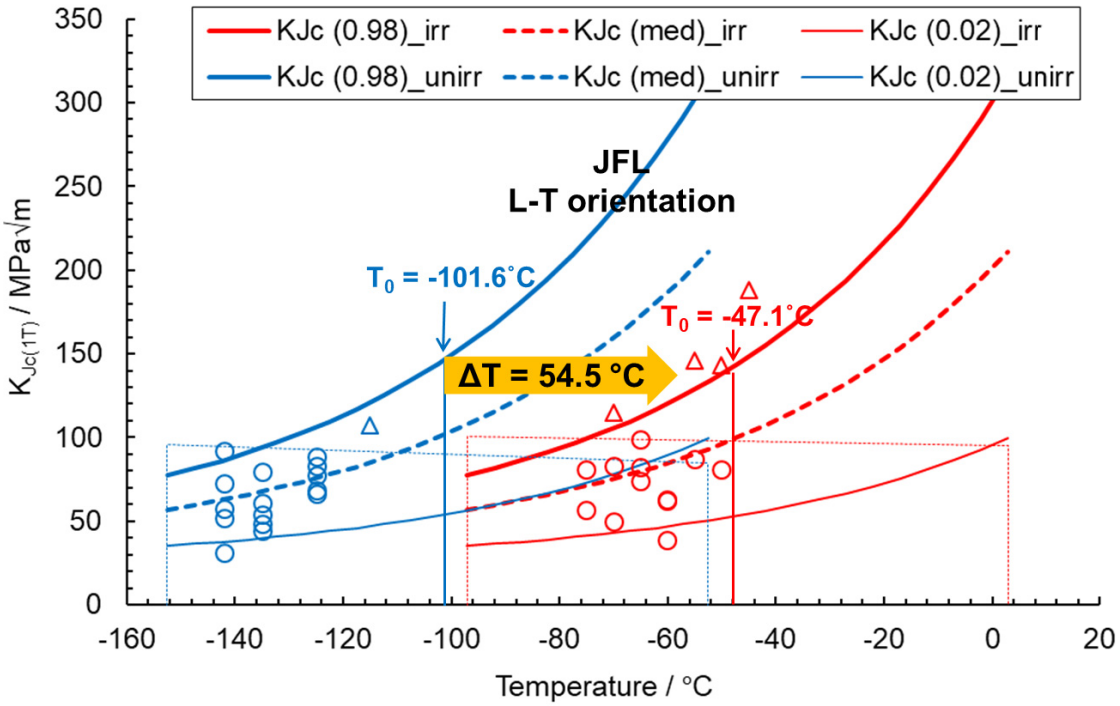

Fig. 10 $K_{\mathrm{Jc(1T)}}$ versus temperature with K_{Jc} median (dashed) along with 98% and 2% tolerance bounds for JFL L-T orientation in the unirradiated and the irradiated states showing the shift in reference temperature

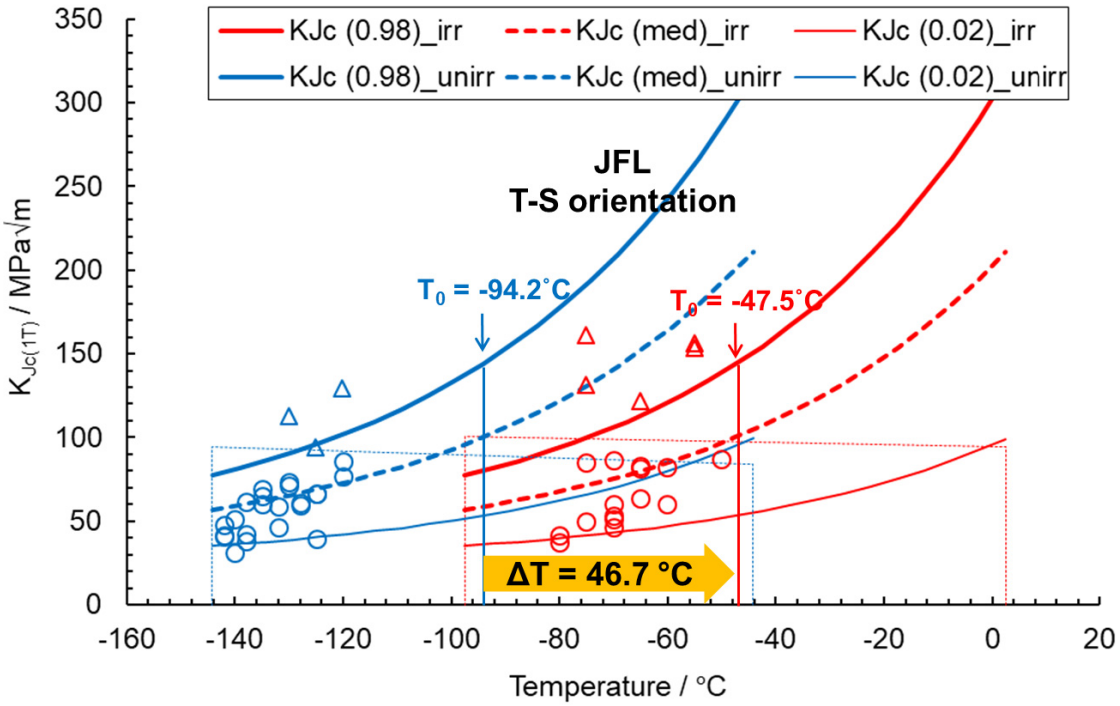

Fig. 11 $K_{\mathrm{Jc(1T)}}$ versus temperature with K_{Jc} median (dashed) along with 98% and 2% tolerance bounds for JFL T-S orientation in the unirradiated and the irradiated states showing the shift in reference temperature

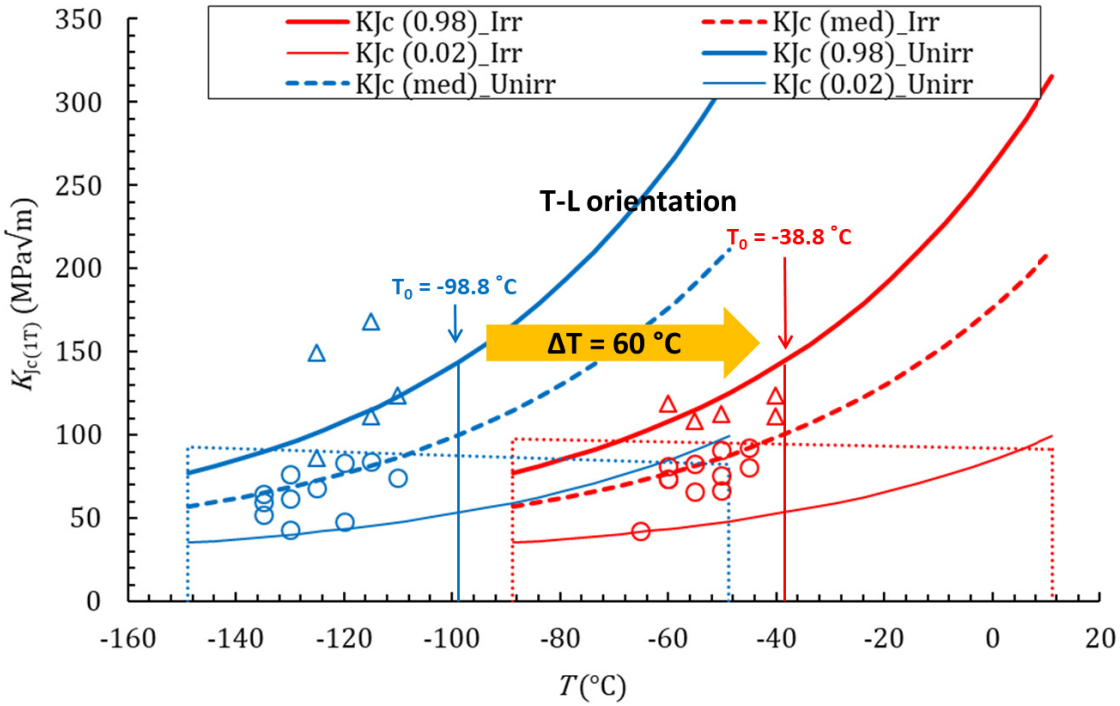

Fig. 12 $K_{\mathrm{Jc(1T)}}$ versus temperature with K_{Jc} median (dashed) along with 98% and 2% tolerance bounds for ANP-3 T-L orientation in the unirradiated and the irradiated states showing the shift in reference temperature

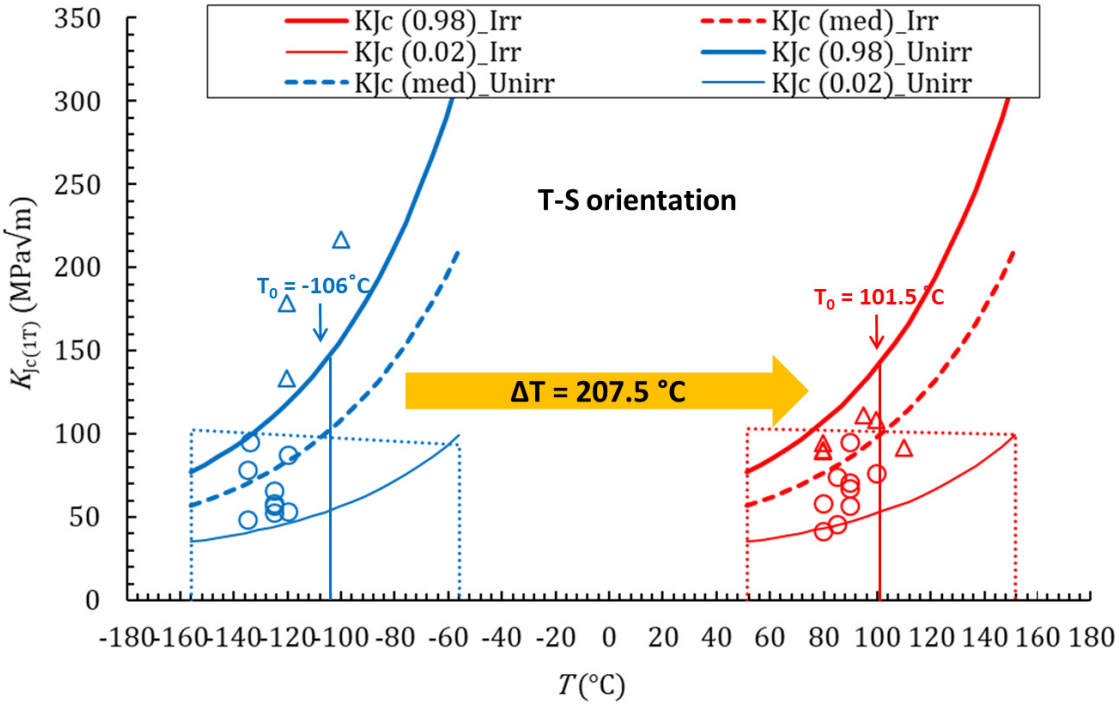

Fig. 13 $K_{\mathrm{Jc(1T)}}$ versus temperature with K_{Jc} median (dashed) along with 98% and 2% tolerance bounds for ANP-6 T-S orientation in the unirradiated and the irradiated states showing the shift in reference temperature

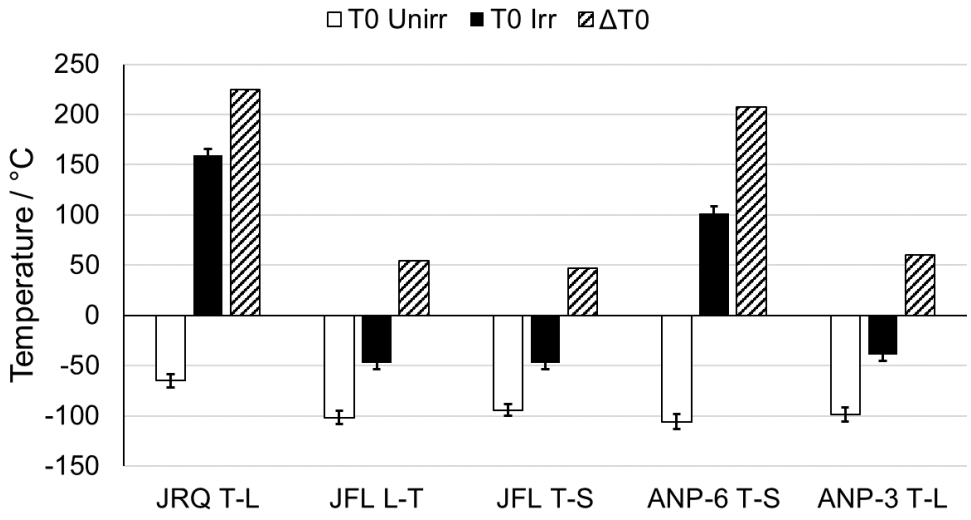

Fig. 14 The reference temperatures (T_0) for all the tested materials in both their unirradiated and irradiated states along with the shift in reference temperatures (ΔT_0).

Table 4 Master Curve results for JRQ and JFL in both unirradiated and irradiated states. The ΔT_0 is calculated between the same orientations.

Material	Condition	Orientation	r	N	$\sum r_i \cdot n_i$	σ K	T_0 °C	ΔT_0 K
3JRQ57	Unirr	T-L	12	12	1.589	6.7	–64.9	--
		T-S	14	16	1.911	6.4	–67.8	--
	Irr	T-L	14	14	1.988	6.4	159.5	224.4
1JFL11	Unirr	L-T	15	16	2.054	6.3	–101.6	--
		T-S	22	25	2.875	5.9	–94.2	--
	Irr	L-T	12	16	1.833	6.7	–47.1	54.5
		T-S	15	20	2.214	6.3	–47.5	46.7
ANP-3	Unirr	T-L	11	16	1.542	6.9	–98.8	--
	Irr	T-L	11	16	1.690	6.9	–38.8	60
ANP-6	Unirr	T-L	7	11	1.048	8.2	–84.7	--
		T-S	9	12	1.286	7.4	–106	--
	Irr	T-S	9	15	1.405	7.2	101.5	207.5

5.2 Comparison of standard Charpy-sized and mini-C(T) specimen

The results of MC testing for the standard Charpy-sized specimens can be found in reference [9]. In Table 5, the reference temperatures and standard deviations determined from the standard Charpy-sized SE(B) specimens and the 0.16T C(T) specimens are listed along with Δθ (the difference between the reference temperatures of standard Charpy-sized and mini-C(T) specimens) for JRQ, JFL and ANP-6. JRQ and JFL were directly manufactured from the standard Charpy-sized specimens and exposed to the same irradiation conditions facilitating a direct comparison. For unirradiated ANP-6, a 1T C(T) specimen instead of a standard Charpy-sized specimen was compared with a mini-C(T) specimen. For the irradiated case of ANP-6, a standard Charpy-sized SE(B) specimen was irradiated with a neutron fluence of 8.36×10^{19} n/cm^2 and compared with a mini C(T) specimen irradiated with 5.6×10^{19} n/cm^2. The reference temperatures of the materials in the unirradiated and the irradiated states is given in Fig. 15 and Fig. 16, respectively. Standard deviations are given as error bars. The reference temperatures of the 0.16T C(T) specimens fall within the error bars of the standard Charpy-sized SE(B) specimens with the same orientation for all the unirradiated and irradiated cases. Standard Charpy-sized and mini-C(T) specimens of different orientations yielded slightly different reference temperatures, but were still within error bars for JRQ and JFL. For ANP-6 however, the

change in the orientation (for both unirradiated and irradiated states) and the change in neutron fluence (for irradiated state) resulted in reference temperatures outside the error bars. This deviation was highest for the irradiated case (Fig. 16).

Table 5 Reference temperatures of standard Charpy-sized SE(B) and 0.16T C(T) specimens along with the standard deviations. The difference between the reference temperatures of standard Charpy-sized and mini-C(T) specimens in also listed (Δθ).

Unirradiated							
Material	Orientation	$T_0 \pm \sigma$ SE(B) (°C)	r SE(B)	N SE(B)	$\sum r_i \cdot n_i$ SE(B)	$T_0 \pm \sigma$ 0.16T C(T) (°C)	Δθ (K)
3JRQ57	T-L	–65.6 ± 6.0	9	10	1.40	–64.9 ± 6.7	0.6
	T-S					–67.8 ± 6.4	2.3
1JFL11	L-T	–105.8 ± 4.7	16	18	2.38	–101.6 ± 6.3	4.2
	T-S					–94.2 ± 5.9	11.6
ANP-6	T-L	–86.1 ± 7.9*	7	7	1.17	–84.7 ± 8.2	1.3
	T-S					–106 ± 7.4	20
Irradiated							
3JRQ57	T-L	164.2 ± 4.9	15	15	1.88	159.5 ± 6.4	4.7
	T-S						
1JFL11	L-T	–45 ± 3.8	22	23	3.35	–47.1 ± 6.7	2.1
	T-S					–47.5 ± 6.3	2.5
ANP-6	T-L	–35.6 ± 7.9**	7	7	1.07		
	T-S					101.5 ± 7.2	65.9

*Obtained from 1T C(T) specimen, **Obtained from specimen irradiated at 8.36 x 10^{19} n/cm^2

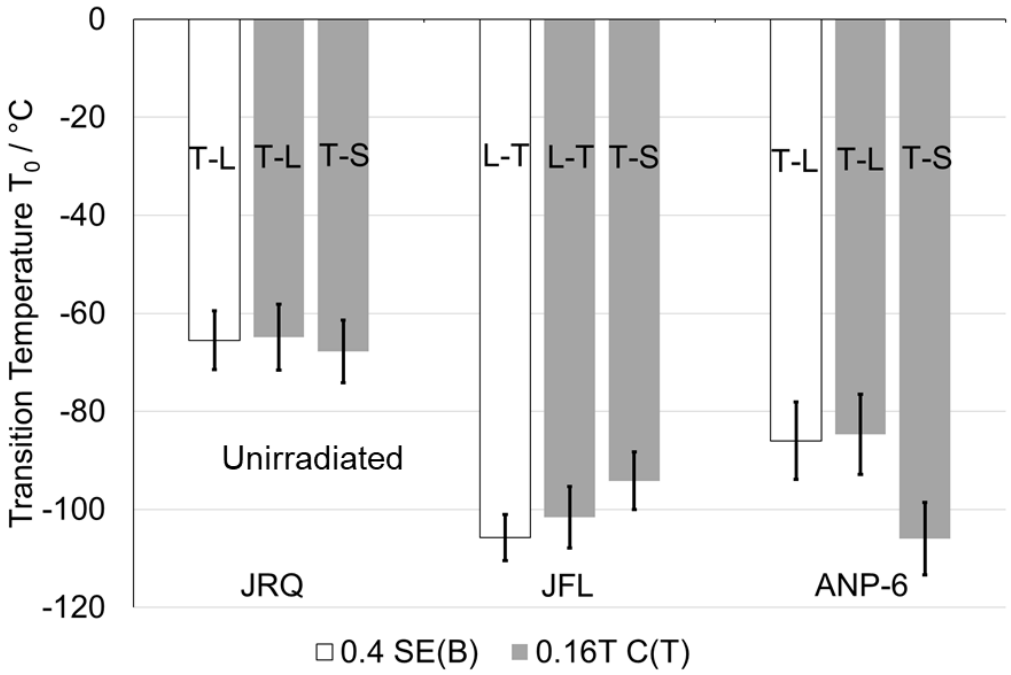

Fig. 15 Reference temperatures for unirradiated materials comparing the standard Charpy-sized SE(B) and 0.16T C(T) specimens.

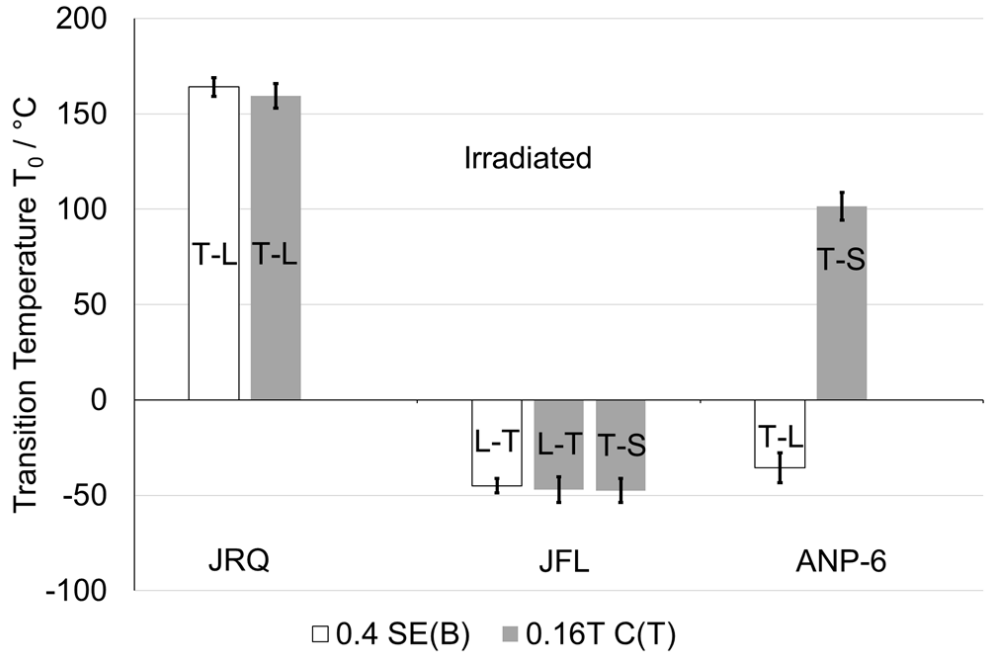

Fig. 16 Reference temperatures for irradiated materials comparing the standard Charpy-sized SE(B) and 0.16T C(T) specimens.

5.3 Fractography

5.3.1 Location of primary fracture initiators

The primary fracture initiation sites were located using SEM as described in section 4.4.1. Fig. 17 shows the fracture toughness K_{Jc} values plotted against the distance to the crack tip. Fracture initiators located at greater distances to the crack front exhibit higher K_{Jc} values and vice-versa. This was true for both the unirradiated and irradiated state. However, the fracture initiators in the irradiated state were located at larger distances from the crack front, especially for JFL and ANP-6, as compared to the unirradiated state. The position of the crack initiator with respect to the side surfaces can be seen from Fig. 18 where the x axis plots the ratio of distance to the side surface to the specimen half width against the fracture toughness K_{Jc}. Fracture toughness values are scattered for all materials. Fracture initiators in the irradiated state were closer to the middle of the specimen as compared to the unirradiated state.

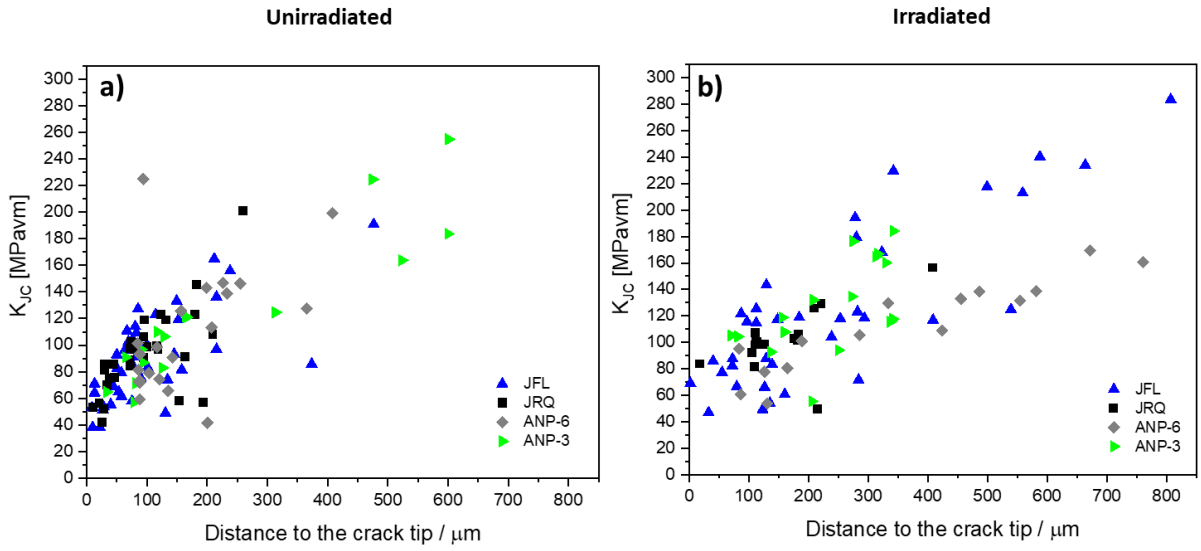

Fig. 17 Fracture toughness K_{Jc} values from Master Curve tests plotted against the distance to the crack tip for all the materials in their a) unirradiated and b) irradiated states.

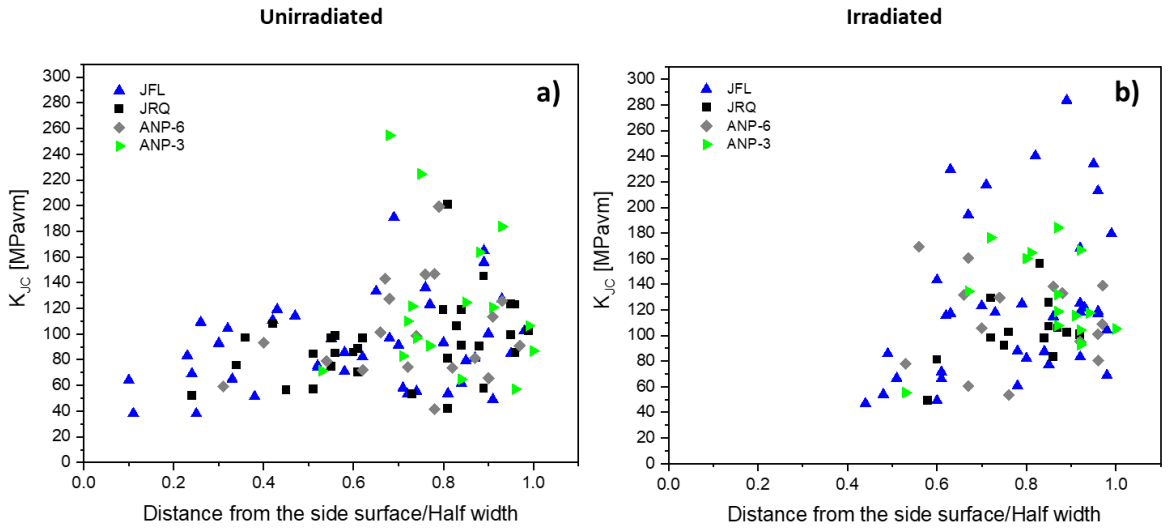

Fig. 18 Fracture toughness K_{Jc} values from Master Curve tests plotted against the ratio of the distance from the side surface to the half specimen width for all the materials in their a) unirradiated and b) irradiated states.

5.3.2 Fracture mode

We selected two samples for each material in a single orientation from a $T - T_0$ range of ≈ –21.1 K ± 1.4 K, since the chances of tests being valid and uncensored at this temperature range was higher. The average statistics of fracture mode from the two samples are considered for each material. Fig. 19 shows the relative fraction of ductile, cleavage and intergranular (IG) fracture mode present in the samples. Relative to the unirradiated state, ductile fracture mode increases the most in irradiated state for ANP-6 followed by JRQ and ANP-3. The ductile fracture mode fraction for JFL remains the same irrespective of the irradiation state. For an increase in the fraction of ductile fracture mode, a corresponding decrease in the fraction of cleavage mode for all materials is observed which follows the same order of decrease as the order of increase in ductile mode. A small fraction of intergranular fracture is observed for JRQ irradiated samples. IG fracture is absent for all other materials irrespective of their irradiation state.

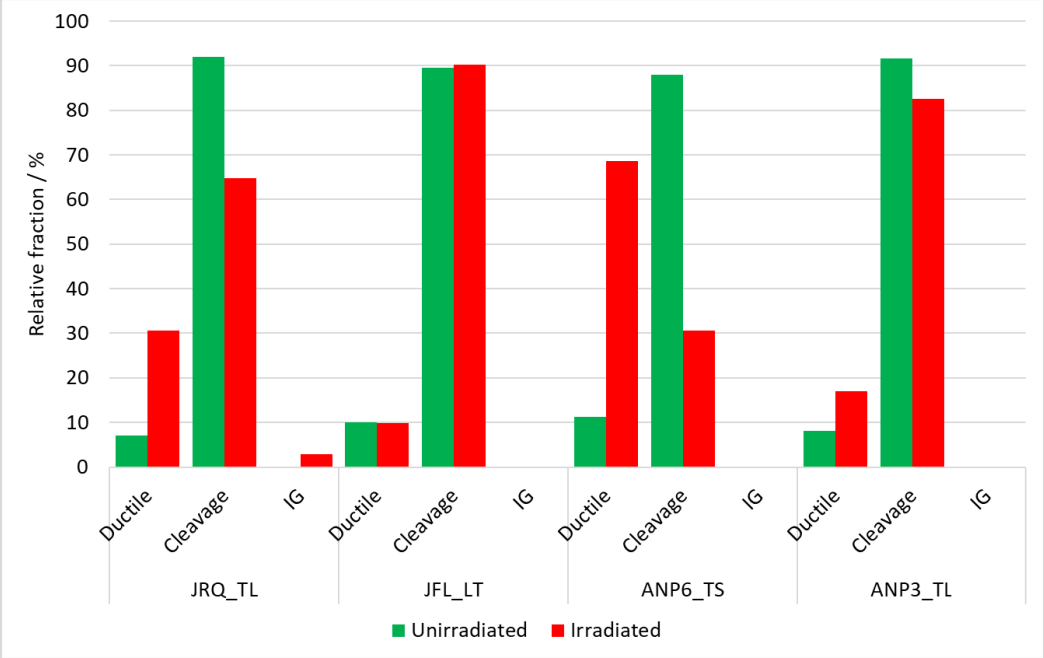

Fig. 19 Relative fractions of different fracture modes visible from the fracture surfaces of all the materials at a $T - T_0$ value of ≈ -21.1 K

Another measure of the extent of ductile fracture mode present in tested sample is the width of the stable crack growth region. We plotted the width of the stable ductile crack growth region against $T - T_0$ in Fig. 20. The closer the samples were tested to the reference temperature, the larger the ductile crack growth region was. In general, irradiated samples from all the material exhibit a larger ductile crack growth region as compared to the unirradiated state. We considered 0.2 mm as the limit for the violation of the $K_{\mathrm{Jc\Delta a}}$ censoring criterion (covered in the next section). This limit was exceeded mostly by ANP-3 and ANP-6 samples.

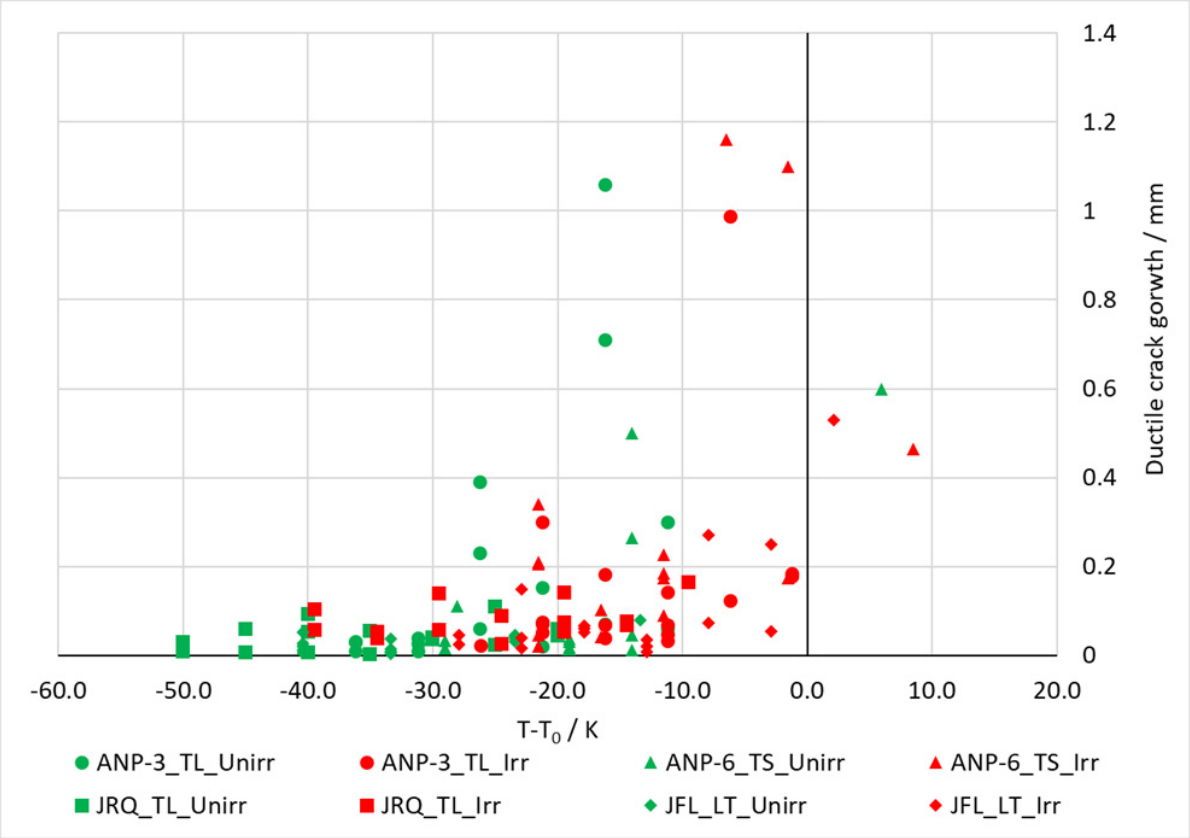

Fig. 20 The width of the ductile crack growth region plotted against $T - T_0$ for all the materials in the unirradiated and the irradiated states

5.4 Censoring statistics

Based on 381 mini-C(T) tests from 11 different materials (Table 2), the absolute number of uncensored and censored tests at each temperature interval are shown in Fig. 21a. The number of tests performed for $T - T_0 < 10$ K were significantly higher than for $T - T_0 > 10$ K. Fig. 21b shows the relative probability of a test being censored at each temperature interval. The weighting factor n_i is highlighted for various temperature intervals as bars on top of Fig. 21b. The cumulative relative censoring probability is ≤ 15 % for $T - T_0 < -25$ K. The relative censoring frequency increases significantly to > 50 % for $T - T_0 > -10$ K [40].

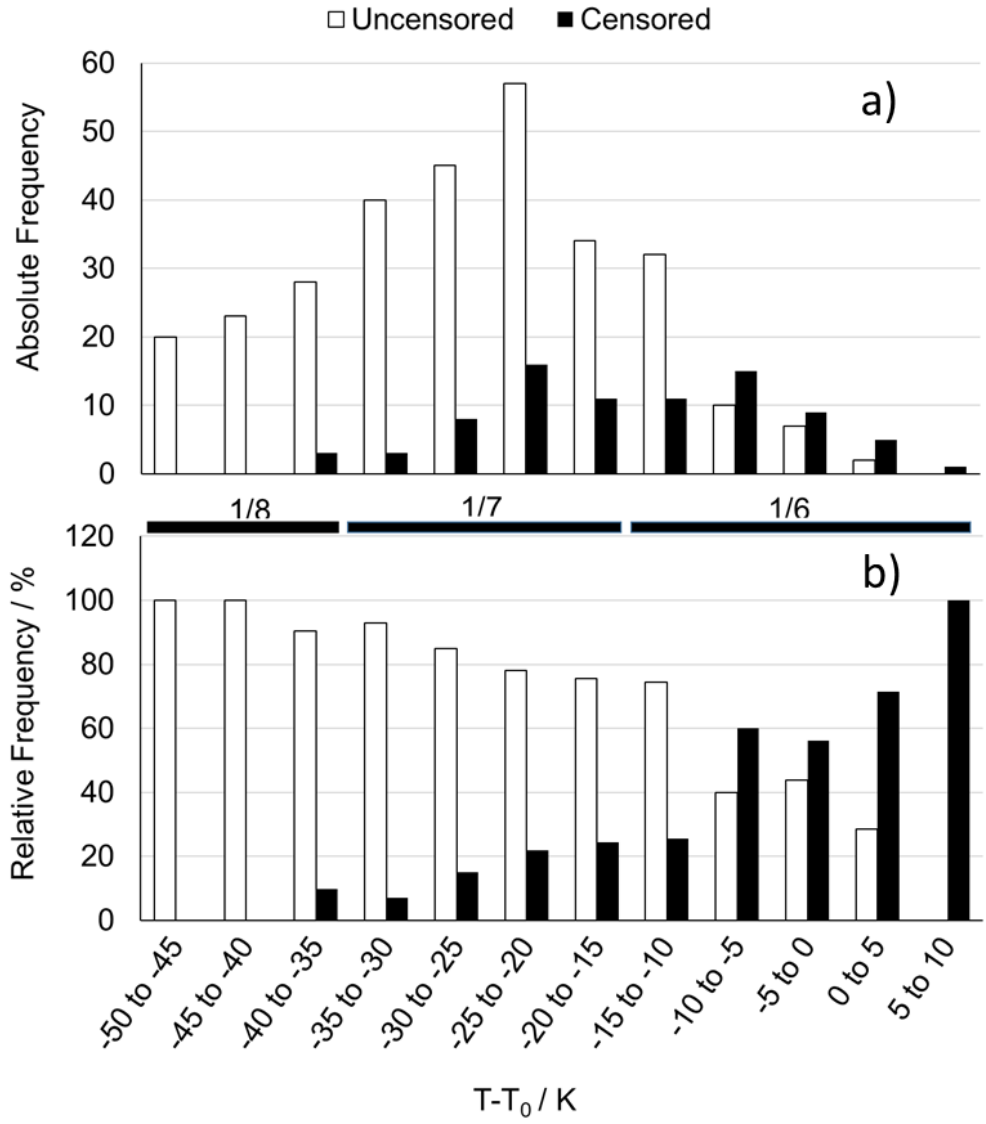

Fig. 21 Absolute a) and relative b) frequencies of uncensored and censored data in temperature intervals of 5 K ranging from -50 to 10 K. In b) the weighting factors (n) are shown for the different temperature ranges (bars on top).

5.5 The stable crack growth censoring criterion

For the verification of the $K_{\mathrm{Jc\Delta a}}$ censoring criterion, we selected 156 tests from the 381 tests listed in Table 2, 89 in the unirradiated and 67 in the irradiated state. The selection was performed taking into consideration that in a test series, at least one test was violating the $K_{\mathrm{Jc\Delta a}}$ criterion (bold values in Table 6). The violation of the $K_{\mathrm{Jc\Delta a}}$ criterion is detected using SEM as mentioned in section 3.4.2. Out of the 156 tests, the K_{Jclimit} criterion is violated in 36 samples while the $K_{\mathrm{Jc\Delta a}}$ criterion is violated in 29 samples as shown in Table 6. The number of samples where both criteria are violated is 23. T_0 is calculated taking into account the violation of both

the K_{Jclimit} and the $K_{\mathrm{Jc\Delta a}}$ censoring criterion (with $K_{\mathrm{Jc\Delta a}}$ in Table 6). It is also calculated for the case when only the K_{Jclimit} censoring criterion is considered (without $K_{\mathrm{Jc\Delta a}}$ in Table 6) i.e. the violation of $K_{\mathrm{Jc\Delta a}}$ censoring criterion is forcefully negated. The ΔT_k (difference between T_0 calculated with and without $K_{\mathrm{Jc\Delta a}}$ censoring criterion) and σ (standard deviation with the $K_{\mathrm{Jc\Delta a}}$ censoring criterion) for different materials are listed in Table 6 as well as highlighted in Fig. 22. The average ΔT_k for these samples was 2.8 °C, which was lower than the average standard deviation of 7.2 °C for these samples [40].

Table 6 List of specimens analysed with the K_{Jclimit} and $K_{\mathrm{Jc\Delta a}}$ censoring criterion along with the T_0 calculated with and without the $K_{\mathrm{Jc\Delta a}}$ censoring criterion. The difference in T_0 from both criteria (ΔT_k) as well as the standard deviation (σ) is also listed. Values in bold represent the specimens selected to verify the $K_{\mathrm{Jc\Delta a}}$ censoring criterion. ***Total and average are calculated from the bold values.**

Material	Condition	Orientation	Testing temperature range $T - T_0$ (K)	r	N	K_{Jclimit} violation	$K_{\mathrm{Jc\Delta a}}$ violation	T_0 (with $K_{\mathrm{Jc\Delta a}}$) °C	T_0' (without $K_{\mathrm{Jc\Delta a}}$) °C	ΔT_k K	σ K
3JRQ57	Unirr	T-L	-50.1 to -20.1	12	12	0	0	-64.9	-64.9	0	6.7
		T-S	**-47.2 to -22.2**	**14**	**16**	**2**	**1**	**-67.8**	**-69.5**	**1.7**	**6.4**
	Irr	T-L	-39.5 to 9.5	14	14	0	0	159.5	159.5	0	6.4
1JFL11	Unirr	L-T	-40.4 to -13.4	15	16	1	0	-101.6	-101.6	0	6.3
		T-S	-47.8 to -25.8	22	25	3	0	-94.2	-94.2	0	5.9
	Irr	**L-T**	**-27.9 to 2.1**	**12**	**16**	**4**	**3**	**-47.1**	**-47.3**	**0.2**	**6.7**
		T-S	**-32.5 to -2.5**	**15**	**20**	**5**	**3**	**-47.5**	**-50.9**	**3.4**	**6.3**
ANP-6	Unirr	**T-L**	**-25.3 to -5.3**	**7**	**11**	**4**	**1**	**-84.7**	**-85.5**	**0.8**	**8.2**
		T-S	**-29 to 6**	**9**	**12**	**3**	**3**	**-106**	**-107.4**	**1.4**	**7.4**
		S-L	-46.8 to -26.8	8	8	0	0	-73.2	-73.2	0	8.2
	Irr	**T-S**	**-21.5 to 8.5**	**9**	**15**	**2**	**6**	**101.5**	**106.2**	**4.7**	**7.2**
ANP-3	Unirr	**T-L**	**-36.2 to -11.2**	**11**	**16**	**4**	**5**	**-98.8**	**-100**	**1.2**	**6.9**
	Irr	**T-L**	**-26.2 to -6.2**	**11**	**16**	**5**	**1**	**-38.8**	**-39.7**	**0.9**	**6.9**
ANP-2	Unirr	S-L	-25.1 to 24.9	7	12	5	0	-54.9	-54.9	0	7.9
		T-S	-25.6 to -15.6	5	6	1	0	-54.4	-54.4	0	9.3
ANP-5	Unirr	**S-L**	**-48 to -28**	**9**	**10**	**1**	**1**	**-22**	**-28.7**	**6.7**	**7.8**
		T-L	-45.9 to -25.9	9	9	0	0	-24.1	-24.1	0	7.8
		T-S	**-43.6 to -23.6**	**9**	**12**	**2**	**3**	**-26.4**	**-33.9**	**7.5**	**7.8**
FZD-4	Unirr	**L-S**	**-28.1 to -8.1**	**8**	**12**	**4**	**2**	**-101.9**	**-104.1**	**2.2**	**7.8**
		L-T	-24.9 to -4.9	10	12	2	0	-115.1	-115.1	0	7.2
		S-T	-42.8 to -22.8	9	10	1	0	-97.2	-97.2	0	7.4
CRIEPI	Unirr	T-S	-30.7 to -10.7	17	22	5	0	-102	-102	0	6.1
Total*				**114**	**156**	**36**	**29**	**Average***		**2.8**	**7.2**

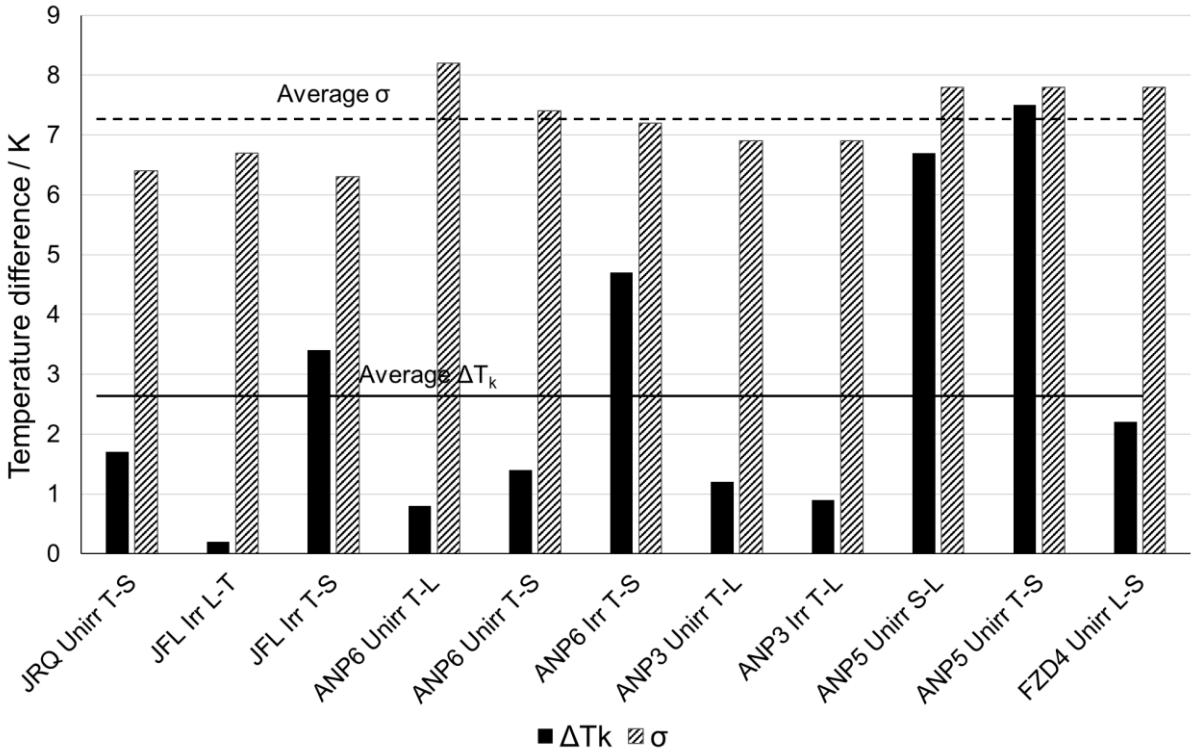

Fig. 22 The ΔT_k and σ values from Table 6 for various materials. The dashed horizontal line indicates the average standard deviation while the solid horizontal line indicates the average temperature difference.

6 Discussion

6.1 Reference temperatures from Master Curve testing

6.1.1 Unirradiated reference temperatures

The reference temperature of unirradiated JRQ comes out to be very close to the T_0 value reported in [13]. Fig. 23 shows the unirradiated reference temperatures of all the materials in different orientations. Only a small variation in T_0, falling within the bounds of the standard deviation, was observed for tests in different orientations for JRQ and JFL. This is due to the microstructure of JRQ and JFL, which were homogeneous and underwent the austenization process resulting in equiaxed grains [41], weakening any texture present by the bainitic transformation. A detailed microstructural analysis of JFL will be performed in another study. The yield strength variation as a function of temperature together with the yield stress values at experimentally determined T_0 values are plotted in Fig. 24 for all the RPV steels. The lowest yield strength at T_0 was obtained for ANP-3 while the highest was obtained for ANP-6.

ANP-3, which is also a base material, contains higher amounts of Mn, Cr and Mo and exhibits lower yield strength values as compared to JRQ and JFL (Fig. 24). The weld material ANP-6, containing higher Ni and lower C contents, exhibits a higher yield strength as compared to the other materials. Additionally, ANP-6 was inhomogeneous which reflected in the varying T_0 obtained for different orientations (Fig. 23).

The equations used for the temperature dependence of yield strength for the RPV steels are mentioned below where the temperature T is in °C and the yield strength is in MPa:

$$\sigma_{JRQ} = 4 \cdot 10^{-8} \cdot T^4 - 2 \cdot 10^{-5} \cdot T^3 + 0.0036 \cdot T^2 - 0.543 \cdot T + 490.29 \quad (1)$$

$$\sigma_{JFL} = 0.0056 \cdot T^2 - 0.3269 \cdot T + 478.93 \text{ valid between } -135\,°C < T < 22\,°C \quad (2)$$

$$\sigma_{JFL} = \sigma_{JFL}(T = 21\,°C) + \frac{55555}{273+T(°C)} - 189 \text{ valid for } T > 22\,°C \quad (3)$$

$$\sigma_{ANP-3} = 349 + 86.7 \cdot \exp(-0.00691 \cdot T) \quad (4)$$

$$\sigma_{ANP-6} = 457 + 545.25 \cdot \exp[-0.00572 * (T + 273)] \quad (5)$$

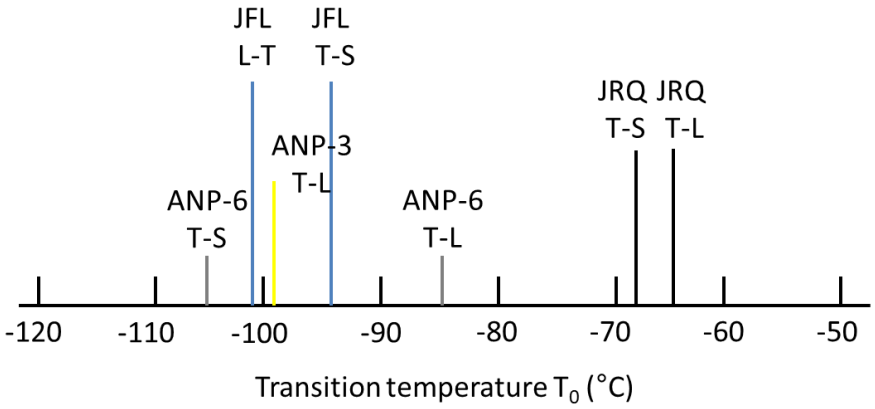

Fig. 23 Unirradiated reference temperatures for all the materials in different orientations

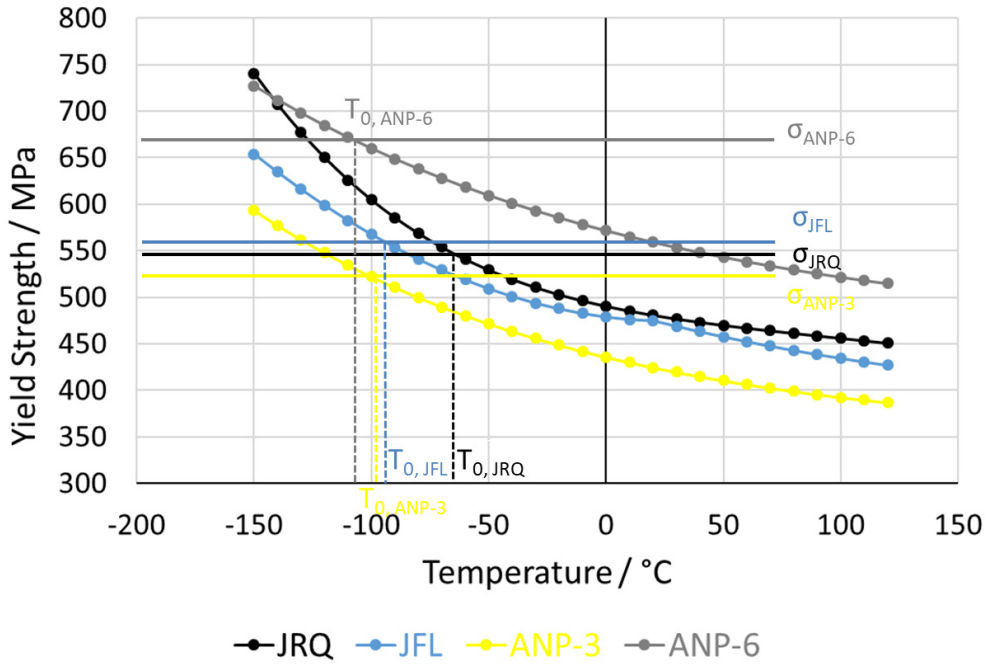

Fig. 24 Yield Stress as a function of temperature for unirradiated RPV steels along with their experimentally obtained T_0 values and their respective yield strengths at T_0.

6.1.2 Shift in reference temperatures

Neutron-irradiation leads to hardening of the material, which translates into an increase in the yield strength. This is often associated with an embrittlement effect represented by an increase in the reference temperature ΔT_0. The increase in yield strength due to neutron irradiation was measured at room temperature for all the materials and was assumed to be the equal at all temperatures. In reality, there could be a gradual decrease in hardening at increasing temperatures up to 350 °C. Similar results were observed for reduced activation ferritic martensitic (RAFM) and ferritic martensitic (FM) steels in [42]. The yield strength variation with temperature of all the irradiated materials could be plotted using the same equations as mentioned in section 6.1.1 with an additional hardening component; the room temperature yield strength increase $\Delta\sigma_{YS}$ (listed in Table 7 and shown in Fig. 25), added to all the temperatures. In Fig. 25, the experimentally determined values of T_0 for the unirradiated as well as the irradiated states of JRQ are indicated with vertical dashed lines which intersect the unirradiated and the irradiated yield strength-temperature curves at σ_{Unirr} and σ_{Irr}, respectively. The difference $\sigma_{Irr} - \sigma_{Unirr}$ gives $\Delta\sigma$ as shown in Fig. 25. It can be seen that the term $\Delta\sigma$

takes into account both the yield strength increase at room temperature due to neutron-irradiation as well as the loss of yield strength at higher temperatures ($T_{0,Irr}$ compared to $T_{0,Unirr}$). $\Delta\sigma$, is therefore a good indicator of the net hardening of a material. The $\Delta\sigma$ values are listed in Table 7 and are plotted against ΔT_0 for all the RPV steels in Fig. 26. JRQ exhibits significantly higher net hardening as well as the highest ΔT_0 (Fig. 14 and Table 4) as compared to the other materials. This is due to the higher amounts of Cu and P in its composition that results in the formation of Cu-rich precipitates and P segregations. This has also been observed in various other studies [1,22–24]. The presence of some amount of intergranular fracture mode in irradiated JRQ (Fig. 19) is an indication of P segregations at the grain boundaries. JFL, which has similar composition to JRQ except the contents of Cu and P, exhibits a relatively smaller ΔT_0 and $\Delta\sigma$. The fact that inhomogeneity does not affect JFL significantly is supported by the fact that the ΔT_0 obtained for different orientations of JFL is similar (Table 4). ANP-3 too exhibits smaller ΔT_0 and $\Delta\sigma$, similar to JFL, despite containing higher Cu and P contents. It might appear that the lower ΔT_0 of ANP-3 is due to the lower neutron fluence, which was approximately one third of the neutron fluence used for JRQ. However, the following argument goes against it. According to the Regulatory Guide 1.99, Revision 2 [43], the relation between the shift in reference temperature ΔRT_{NDT} and neutron fluence for western RPV steels is given by Eq. 6.

$$\Delta RT_{NDT} = CF \cdot \Phi^{(0.28-0.1\log\Phi)} \quad (6)$$

Where CF is the chemical factor defined as a function of the Cu and Ni weight percent ($CF = 470 \cdot C_{Cu} + 350 \cdot (C_{Cu} \cdot C_{Ni}) - 10$) and Φ is the neutron fluence in 10^{19} n/cm^2 (E > 1 MeV). We obtain a ΔRT_{NDT} of 118.2 K for ANP-3 with a neutron fluence of 3.9 × 10^{19} n/cm^2 which is higher than the experimentally determined ΔT_0 of 60 K. Similar discrepancies were also found in [30]. For a neutron fluence of 9.82 × 10^{19} n/cm^2, which is similar to that of JRQ, Eq. 6 for ANP-3 gives a ΔRT_{NDT} of 132.3 K. This is not as high as the ΔT_0 obtained experimentally for JRQ (224.4 K). Therefore, low neutron fluence is not the only reason for the small ΔT_0 for ANP-3. A detailed microstructural investigation is needed to answer this, which is beyond the scope of the present work.

Despite exhibiting a large ΔT_0 comparable to that of JRQ, ANP-6 exhibits a relatively low $\Delta\sigma$ value, similar to JFL and ANP-3 (Fig. 26). This is due to the interplay between the yield strength increase at room temperature and decrease in yield strength with increasing temperature as shown in Fig. 25 for ANP-6 and JRQ. ANP-6, which exhibits higher yield strength values in the unirradiated state as compared to JRQ (Fig. 24), experiences less irradiation induced hardening as compared to JRQ. Similar results were reported in [42] where RAFM steels with higher yield strength exhibited lower irradiation induced hardening as compared to the RAFM steels with lower yield strength. This however, does not mean that ANP-6 does not embrittle. On the contrary, a ΔT_0 of 207.5 K indicates severe embrittlement. The low net hardening $\Delta\sigma$ of ANP-6 is a consequence of a high shift in reference temperature ΔT_0 and a moderate irradiation hardening $\Delta\sigma_{YS}$ (as compared to JRQ). Low net hardening means that the fracture in the irradiated condition is associated with relatively low flow stress which promotes plastic deformation, see section 4.2.

ErickssonKirk [44,45] provided a detailed analysis of thermal and athermal aspects of dislocation mobility and their effects on fracture toughness. One of the main conclusions was, that the upper shelf (ductile) fracture toughness decreases with increasing T_0 and thereby T_0 approaches the upper shelf temperature T_{US}, which is the intersection of the master curve $K_{Jc}(T)$ and the ductile initiation curve $J_{Ic}(T)$. Also, from this point of view, one can expect significant plastic deformation and even crack growth in irradiated ANP-6. In this context, $\Delta\sigma$ represents the difference between thermal ($\Delta\boldsymbol{\sigma_T}$) and athermal ($\Delta\boldsymbol{\sigma_{YS}}$) components of flow stress for a material.

Table 7 The values of the shift in reference temperature ΔT_0 together with the net hardening $\Delta\sigma$ values, the room temperature yield strength increase due to irradiation $\Delta\sigma_{YS}$ and the loss of yield strength ($\Delta\sigma_T$) between $T_{0,Unirr}$ and $T_{0,Irr}$ for all the materials

Material	ΔT_0 K	$\Delta\sigma$ MPa	$\Delta\sigma_{YS}$ MPa	$\Delta\sigma_T$ MPa
JRQ	224.4	250	358.6	106.9
JFL	46.7	120	170.1	52.3
ANP-3	60	110	174	58.2
ANP-6	207.5	130	262	145.7

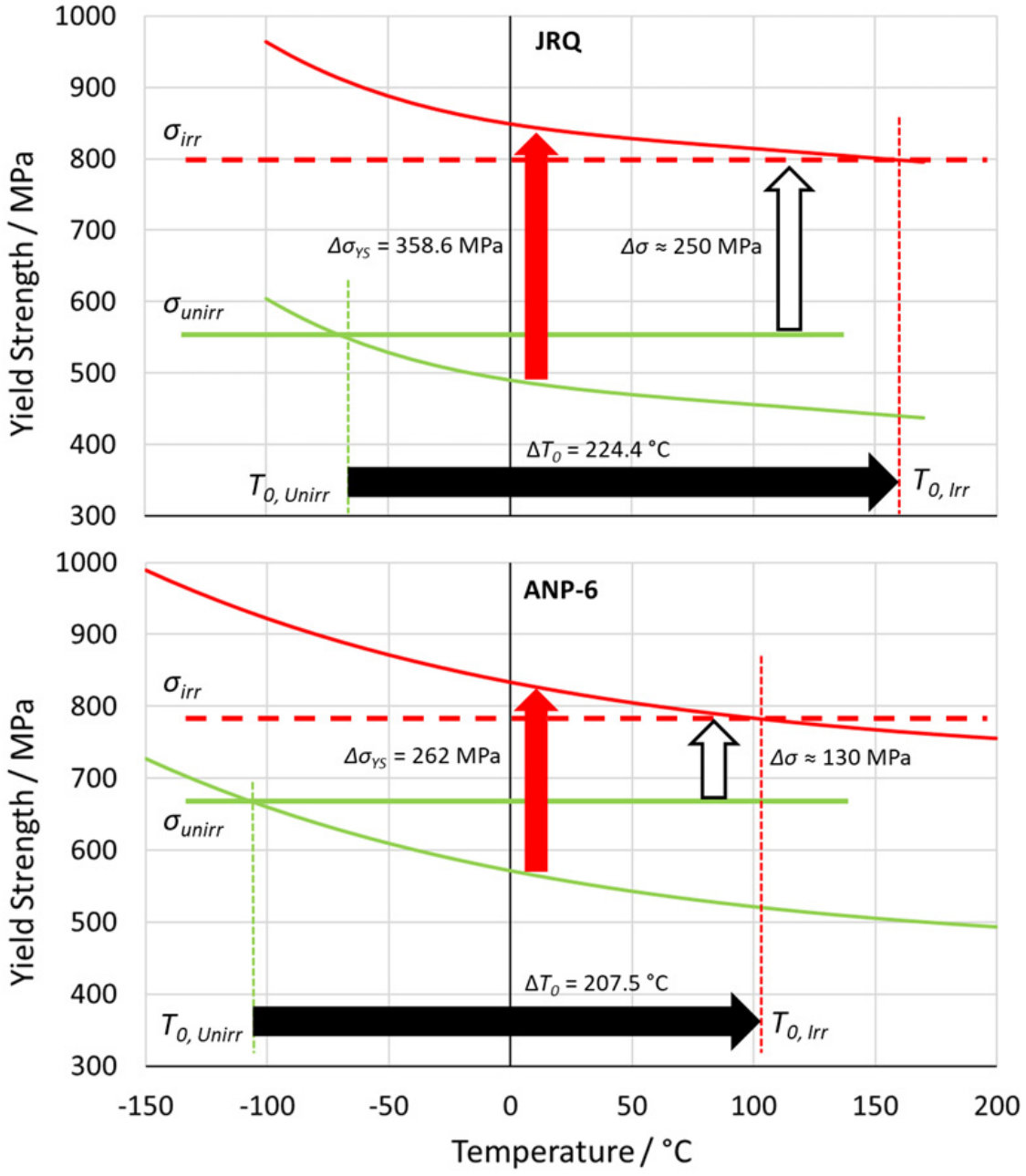

Fig. 25 A plot of yield strength variation as a function of temperature for JRQ and ANP-6 in both the unirradiated and irradiated states, the reference temperatures of both the states and the shift in reference temperature as a result of embrittlement. The increase in yield strength ($\Delta\sigma_{YS}$) after irradiation at RT and the net hardening ($\Delta\sigma$) are marked as well.

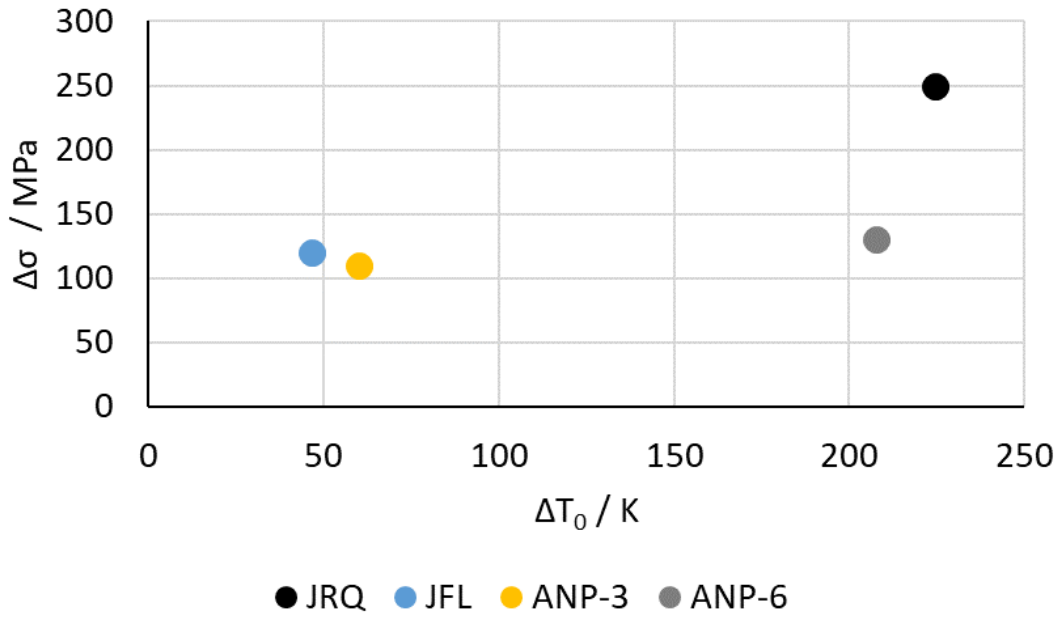

Fig. 26 A plot of the net hardening $\Delta\sigma$ values against ΔT_0 for all the RPV steels

6.1.3 Fracture mode analysis

A plot of $\Delta\sigma_{YS}$, which represents the irradiation hardening at room temperature and $\Delta\sigma_T$, which represents the loss of yield strength between $T_{0,Unirr}$ and $T_{0,Irr}$ also supports the arguments from the previous section (Fig. 27). JRQ exhibits the highest $\Delta\sigma_{YS}$ while ANP-6 exhibits a lower $\Delta\sigma_{YS}$ and the highest $\Delta\sigma_T$. This indicates lower irradiation hardening and a higher degradation of yield strength for ANP-6, which suggests a higher amount of plasticity. This ductile behaviour is also clear from Table 6 where six samples violate the $K_{\mathrm{Jc\Delta a}}$ censoring criteria. The fracture surfaces of irradiated ANP-6 specimens, which exhibit extensive ductile regions, also confirm this. An example of the fracture surface of an ANP-6 irradiated sample is shown in Fig. 28, which shows a large ductile region consisting of dimples followed by cleavage fracture region consisting of facets and river lines (shown in inset). Our finding that ANP-6 exhibits the highest increase in ductile fracture mode behavior after neutron irradiation (Fig. 19) supports the fact that ANP-6 experiences significantly lower irradiation hardening as compared to JRQ and exhibits higher plasticity. In this context, a high value of $\Delta\boldsymbol{\sigma_T}/\Delta\boldsymbol{\sigma_{YS}}$) can be understood as an indicator for ductile fracture appearance.

Caution must however be taken while interpreting the embrittlement of a material from the ductile fracture surfaces alone, since we have observed from the previous section that ANP-6

exhibits a high ΔT_0 value and is severely embrittled. Similar was the case for tensile tests with neutron irradiated RAFM steels, which resulted in ductile fracture surfaces and low loss of reduction in area [42]. This was contradictory to the fracture toughness testing which revealed a high ΔT_0. Fracture toughness methods of determining ΔT_0 are therefore considered the safest way to evaluate the embrittlement of engineering materials with imperfections.

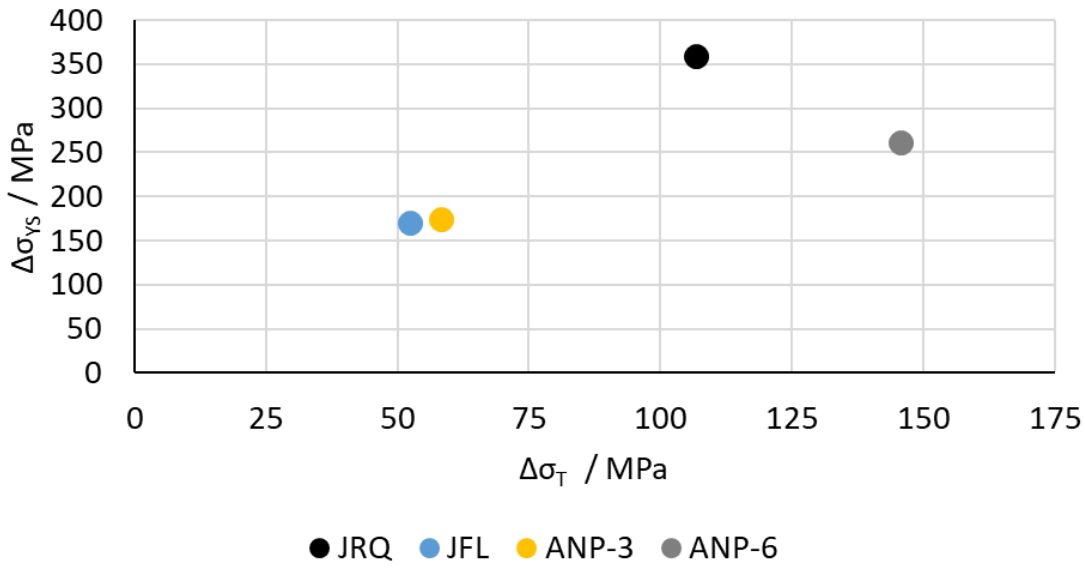

Fig. 27 A plot of increase in yield strength due to irradiation hardening ($\Delta\sigma_{YS}$) versus degradation in yield strength due to increase in temperature ($\Delta\sigma_T$) for all the RPV steels.

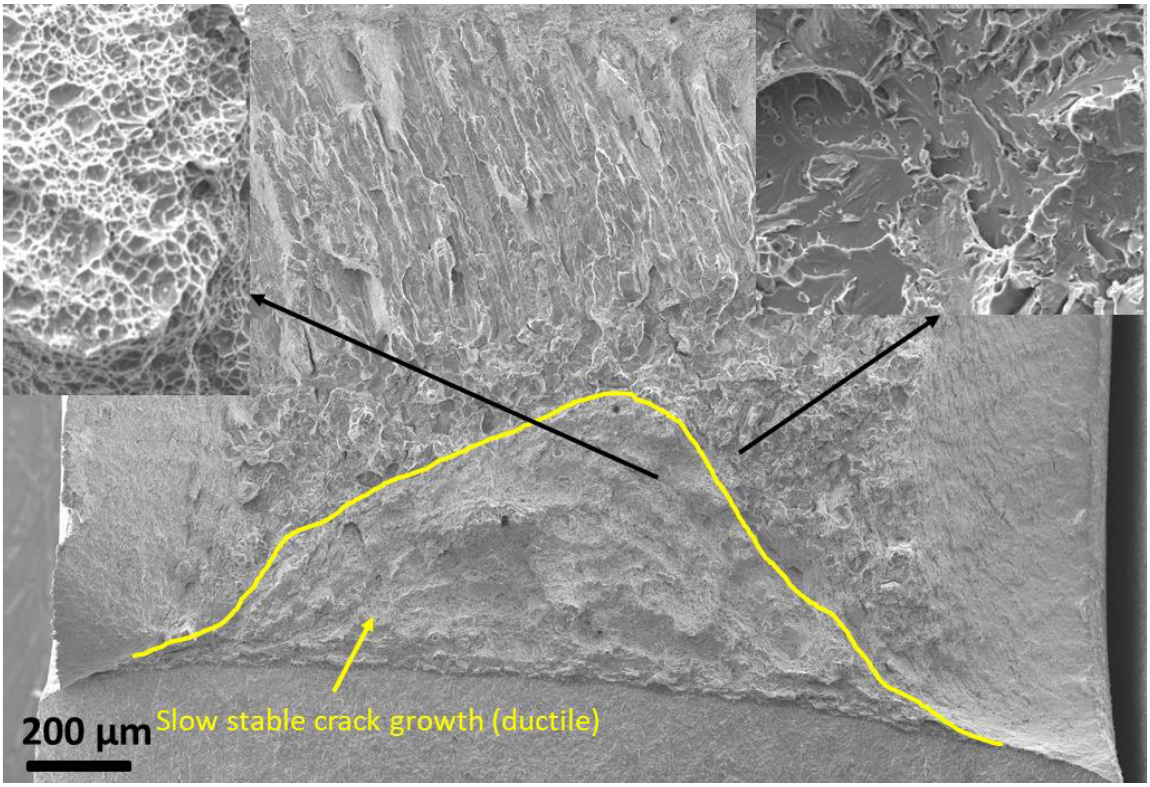

Fig. 28 SEM image of an irradiated ANP-6 sample tested at 100 °C showing a large slow stable crack growth region consisting of dimples followed by a cleavage fracture region (magnified views shown in inset).

6.2 Comparison between standard Charpy-sized and mini-C(T) specimens

6.2.1 Unirradiated state

The difference between the T_0 of standard Charpy-sized and mini-C(T) specimen (Δθ) in the T-L orientation came out to be 0.6 K for JRQ unirradiated specimen (Table 5) which is similar to the difference reported by [13]. The difference between standard Charpy-sized and the mini-C(T) specimen tested in the unirradiated T-S orientation (2.3 K) was also within the standard deviations of both SE(B) (6.0 K) and mini-C(T) specimen testing (6.4 K) (Fig. 15). A T_0 higher by ≈ 10 K was reported in [14] for JRQ using mini-C(T) as compared to standard Charpy-sized specimens.

For JFL, a T_0 higher by 4.2 K and 11.6 K was obtained for the L-T and T-S oriented mini-C(T), respectively as compared to the L-T oriented standard Charpy-sized specimen. While the Δθ for the L-T orientation (4.2 K) is within the bounds of the standard deviation of the mini-C(T) test series (6.3 K), the Δθ for the T-S orientation (11.6 K) is close to the cumulative standard

deviations of the mini-C(T) and standard Charpy-sized specimen tests (Fig. 15). Miura and Soneda reported similar T_0 for mini-C(T) and standard Charpy-sized specimens for JFL [14].

The tests for unirradiated ANP-6 were performed on 1T C(T) specimens and compared with mini-C(T) specimens giving a Δθ of 1.3 K and justifying the works of [13–19] where similar T_0 values were reported for mini- and larger-C(T) specimens. A high Δθ of 20 K for unirradiated mini-C(T) in the T-S orientation highlights the inhomogeneity in the weld material (Fig. 15).

6.2.2 Irradiated state

Similar compatibility was also observed for the irradiated specimens in all the orientations for JRQ and JFL where a slightly lower T_0 was obtained for mini-C(T) as compared to standard Charpy-sized specimens (Table 5 and Fig. 16) thus demonstrating the validity of the application of mini-C(T) specimens. A slightly lower T_0 for irradiated mini-C(T) specimen was also obtained in [13] where the neutron fluence was an order of magnitude lower compared to the present study.

For ANP-6, the changes in irradiation conditions as well the orientation resulted in a significantly large Δθ of 65.9 K (Table 5 and Fig. 16). As discussed in section 6.1.2, the change in neutron fluence affects the shift in the reference temperature in a minor way. The dominant contribution to this large Δθ comes from the change in orientation as ANP-6 weld material is inhomogeneous. Depending on the location of the weld from where the specimen was extracted, the material exhibits varying microstructure and mechanical properties.

6.3 The location of fracture initiators

6.3.1 Distance from the crack front

The fact that the fracture toughness, represented in terms of the K_{Jc} value, is independent of neutron irradiation is depicted in Fig. 29 which shows a processed version of Fig. 17 with only tests conducted at a temperature range of $-35\ °C\ < T - T_0 < \ -15\ °C$. This temperature range was selected as a large number of tests were performed in this range for both the unirradiated and irradiated states, thus providing a better picture of the statistics independent of the effect of variation of the test temperature.

It is clear from Fig. 29 that higher K_{Jc} values are reported at larger distances of the fracture initiators to the crack tip for both the unirradiated and irradiated states. Similar results were also observed by [10,26,27]. This is because the crack tip stresses at larger distances from the crack tip are smaller as compared to the stresses near the crack tip [46]. FEM calculations performed in HZDR reported similar findings as seen in Fig. 30, which shows the normal stresses ahead of the crack tip plotted against the distance to the crack tip for increasing K_I values. Assuming the fracture stress σ_f of a particular kind of fracture initiator to be 1800 MPa (dotted line), the local normal stresses (S_{yy}) ahead of the crack tip at high K_I values ($K_I = 100\ MPa\sqrt{m}$) exceeds the fracture stress even at larger distances to the crack tip (*x* = 30 µm to 104 µm). For lower K_I values ($K_I = 40\ MPa\sqrt{m}$), the fracture stress is exceeded at distances closer to the crack tip (*x* = 12 µm to 20 µm). This suggests that as the crack front propagates with an associated increase in the K_I value, the possibility of fracture occurring at larger distances from the crack front also increases. The stress profiles in Fig. 30 correspond to the plastic properties of the unirradiated material JRQ at –65 °C.

From Fig. 29 it seems like the fracture initiators in the irradiated samples are located at greater distances to the crack tip as compared to the unirradiated samples. However, the data in Fig. 29 includes the stable ductile crack growth region before the cleavage fracture. This region tends to increase with increasing testing temperatures as shown in Fig. 20. Similar results were found in [27]. If we remove the stable ductile crack growth region while calculating the distance of the initiator from the crack front, the plot looks different as shown in Fig. 31. Here, the crack tip stress profile is considered for a crack tip that starts cleavage fracture at the end of the ductile crack growth region. From Fig. 31 it is clear that there is no significant difference between the locations of the fracture initiators in the irradiated state as compared to the unirradiated state.

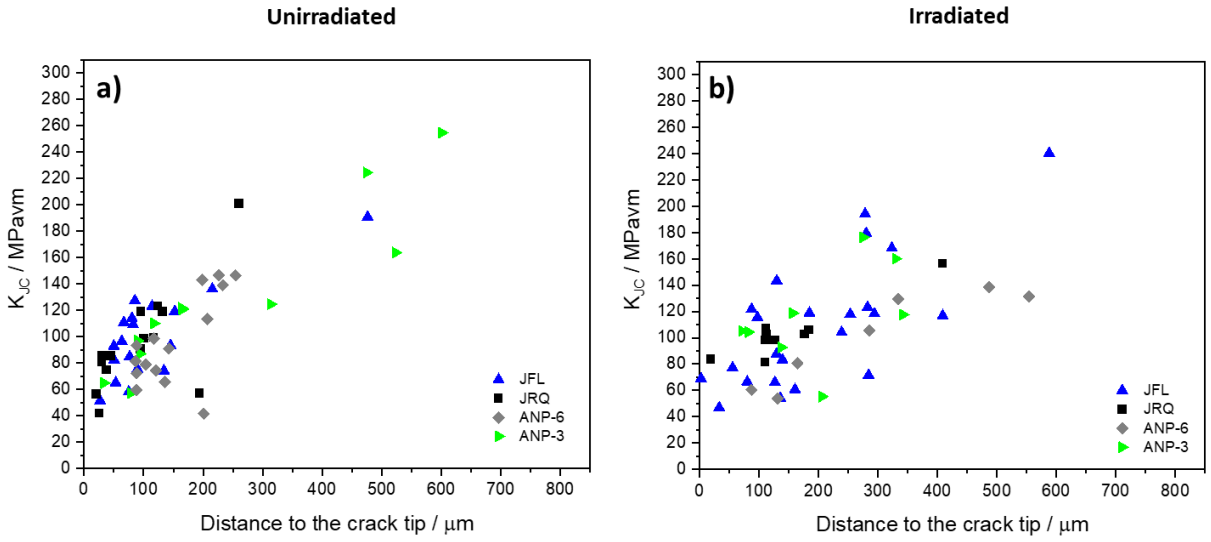

Fig. 29 A processed version of Fig. 17 with data points belonging to the temperature range $-35\ °C\ < T - T_0 <\ -15\ °C$

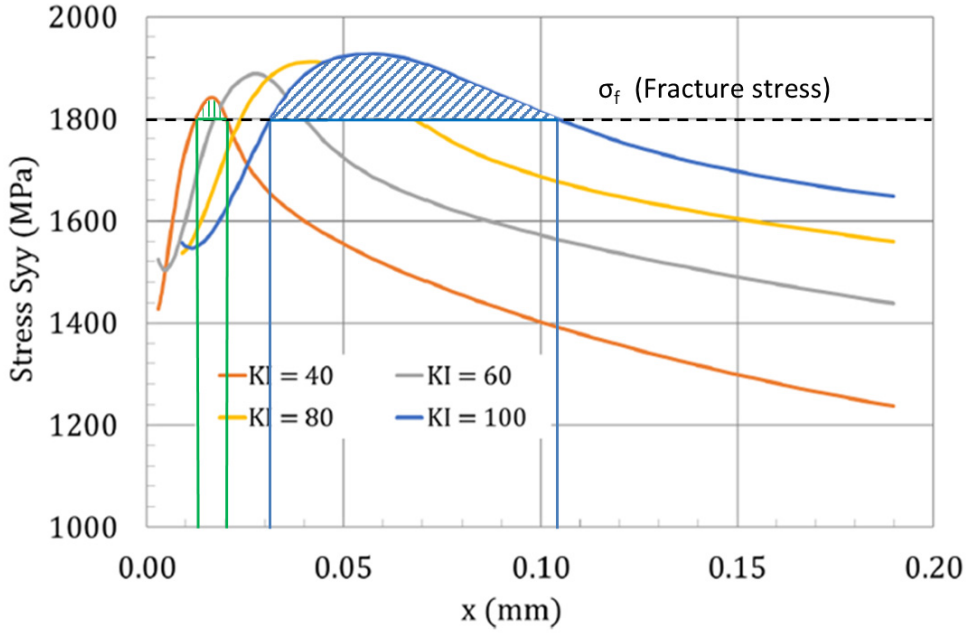

Fig. 30 Stress profiles ahead of the crack tip for increasing stress intensity factors. The fracture stress is assumed 1800 MPa. The shaded area represents the regions where the local normal stresses exceed the fracture stress for a low and a high K_I value.

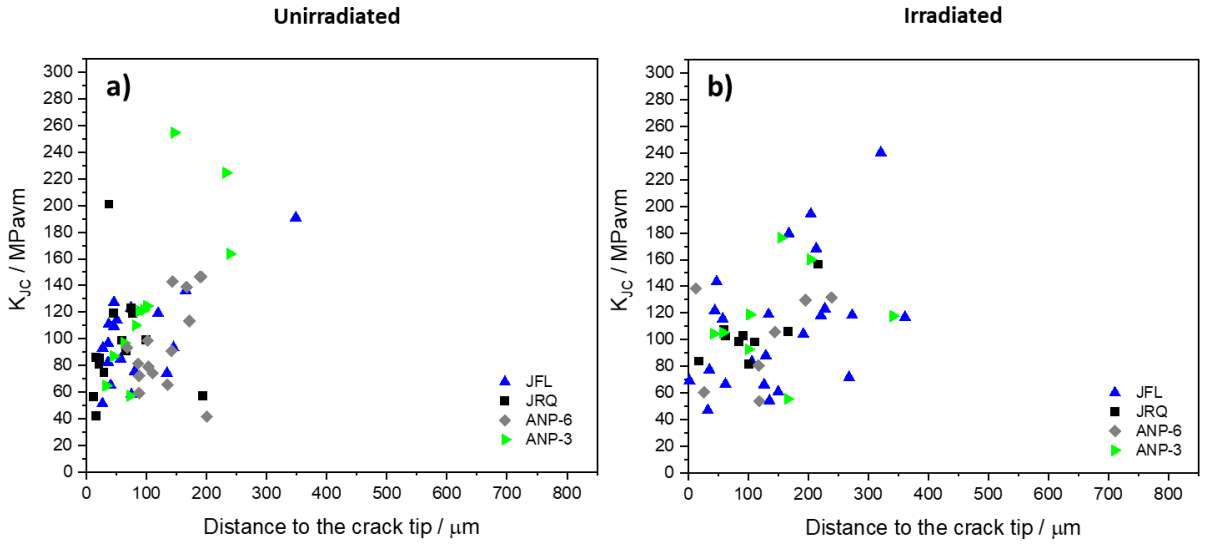

Fig. 31 A processed version of Fig. 29 without the consideration of the ductile crack growth region.

6.3.2 Distance from the side surface

In order to avoid the effect of varying testing temperatures, we process Fig. 18 by select the temperature range of $-35\,°C\ < T - T_0 < -15\,°C$, where a large number of tests were performed, and obtain Fig. 32. Since stress triaxiality is the highest at the middle of the sample, larger stresses are expected in the middle as compared to the sides of the sample as shown in Fig. 33 which shows the transverse stress through the thickness of a non-side-grooved and side-grooved specimen [46]. For a non-side-grooved sample, the plane strain region is restricted in the middle of the sample and a wider plane stress region is located at the sides of the sample as shown in Fig. 33. The local stress values tend to exceed the initiator fracture stress in the middle of the sample rather than those located close to the sides of the sample. For side-grooved samples, the plane stress or the low triaxiality region is restricted to a narrow strip close to the sides of the samples and the plane strain region is extended from the middle towards the sample edges. This results in an even distribution of fracture initiators across the thickness of the sample (Fig. 32a). Similar to our findings, Wallin [19] found that side grooving had a clear but not a dramatic effect on the location of the fracture initiators.

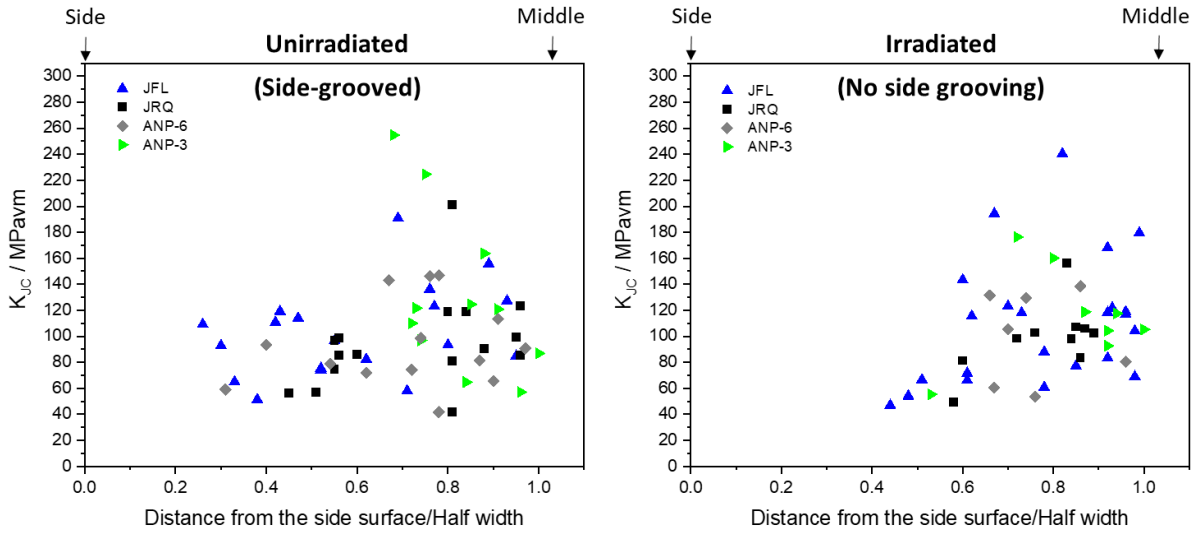

Fig. 32 A processed version of Fig. 18 with data points belonging to the temperature range $-35\ °C\ < T - T_0 < -15\ °C$

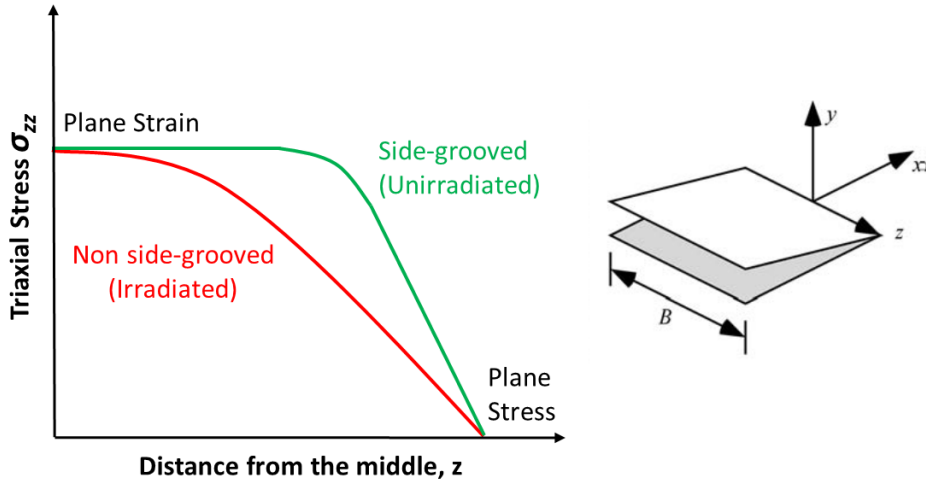

Fig. 33 Variation of transverse stress through the thickness of a specimen indicating plane strain and plane stress regions for non-side-grooved and side-grooved specimens. Schematic modified from [46].

6.4 Statistically based concept for optimum test temperature selection

In the current version of ASTM E1921 (section 10.3), the selection of test temperatures is discussed on a non-quantitative basis. Moreover, the suggestions do not consider the censoring behavior of Mini-CT specimens (which is different from standard Charpy-sized specimens). This may lead to an unnecessarily high number of tests required for a valid T_0-evaluation. The proposed procedure aims at optimizing the use of available Mini-CT samples. Based on the censoring statistics presented in section 5.4, the probability, that a test datum at a certain

temperature will be censored (i.e., $K_{\mathrm{Jc}} > K_{\mathrm{Jclimit}}$ or $K_{\mathrm{Jc}} > K_{\mathrm{Jc\Delta a}}$), can empirically be approximated by a tanh-fit as follows [40]:

$$P_{\mathrm{c}} = 0.5 + 0.5 \cdot \tanh[c \cdot (T - T_0 + T_{\mathrm{sh}})] \tag{7}$$

The tanh-fit is shown in Fig. 34. The relative frequencies from Fig. 21b were used. The obtained fitting parameters are $c = 0.056$ and $T_{\mathrm{sh}} = 7.9$ K, using the complete data set of 381 tests.

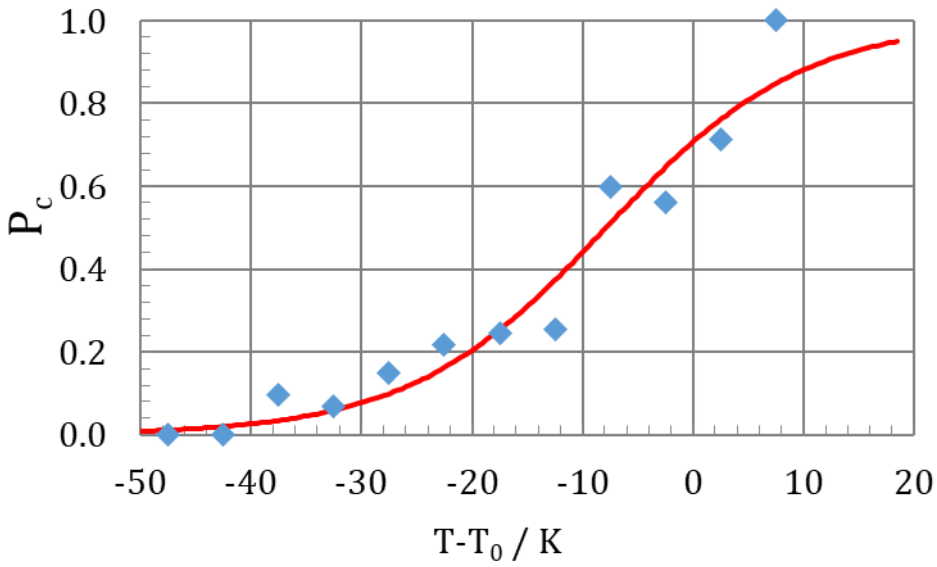

Fig. 34 Tanh-fit of the censoring probability plotted against $T - T_0$

By means of this analytical description of the censoring probability, a statistically based strategy for the selection of test temperatures can be established. The temperatures of the first 3-5 tests have to be selected on the basis of the expected reference temperature. The temperature interval $T_{0,\mathrm{exp}} - 30\ \mathrm{K} < T < T_{0,\mathrm{exp}} - 25\ \mathrm{K}$ is a reasonable choice. Based on these first few data points, a preliminary T_0 can be calculated. The selection of the temperature of the next test is based on a target censoring probability:

$$T = T_0 - T_{\mathrm{sh}} + \frac{1}{c} \cdot \arctan\left[\frac{P_{\mathrm{c,trg}} - 0.5}{0.5}\right] \tag{8}$$

which corresponds to equation (7) rearranged for solving T. The target censoring probability $P_{\mathrm{c,trg}}$ is chosen in dependence of two parameters, $s_{rn} = \sum r_i n_i$ and r/N, calculated from the currently available test data (where *r* is the number of uncensored valid data and N is the total

number of valid data; as for s_{rn}, r_i and n_i cf. ASTM E1921, section 10.3) [28]. The following approach is used:

$$P_{c,trg} = 0.05 + 0.9 \cdot \left[\min\left(\frac{s_{rn}}{3}, 1\right)\right]^{p} \cdot \left[\frac{r}{N}\right]^{q} \tag{9}$$

i.e., $0.05 \leq P_{c,trg} \leq 0.95$. The parameters are $p = 0.7$ and $q = 1.1$, which ensures that the following condition is fulfilled:

$$P_{c,trg} < 0.5 \quad \forall \quad s_{rn} < 1 \text{ and } r/N < 0.5 \tag{10}$$

The target censoring probability is shown in Fig. 35. The procedure based on equations (8) to (10) is repeated after each new test. This concept quantifies the balance between the two competing aspects of temperature selection: testing close to T_0 and avoidance of censoring.

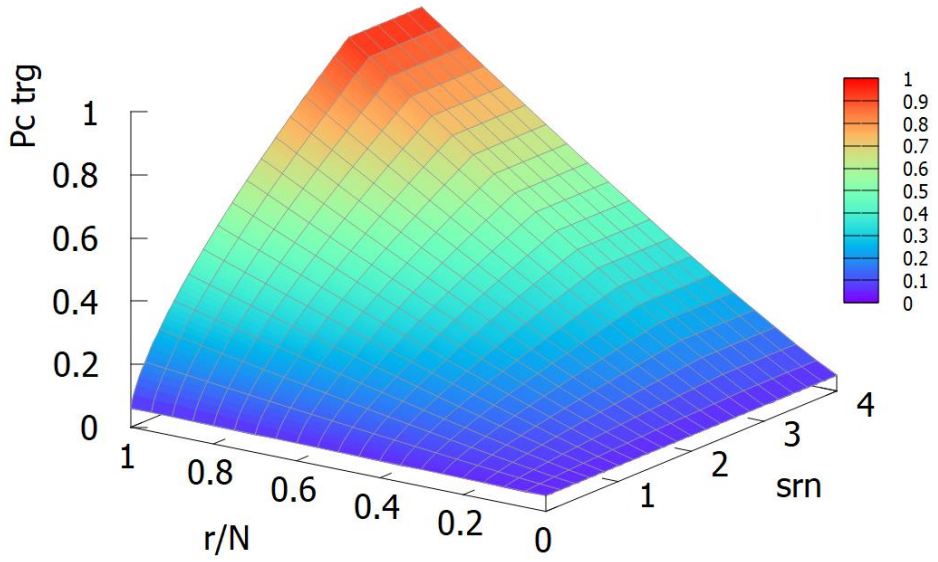

Fig. 35 Target censoring probability as function of s_{rn} and r/N

6.5 The impact of stable crack growth censoring criterion on T_0

At testing temperatures close to T_0, the K_{Jclimit} and the $K_{\mathrm{Jc\Delta a}}$ censoring criteria both tend to be violated. As seen from the results in Table 6, there are 23 samples where both the criteria are simultaneously violated. The inclusion of $K_{\mathrm{Jc\Delta a}}$ censoring criterion results in a small increase in T_0 as compared to the case when only the K_{Jclimit} censoring criterion is considered. The only exception is ANP-6 irradiated specimen. Since this increase (ΔT_k) falls below the standard deviation of individual Master Curve tests (Fig. 22), it is reasonable to say that the impact of the slow stable crack growth censoring criterion on T_0 is insignificant. Therefore, to make the determination of T_0 simpler and to avoid additional time-consuming analysis of the fracture surface, the $K_{\mathrm{Jc\Delta a}}$ censoring criterion could be removed. The removal of this criteria however, results in more conservative values of T_0 which is generally not desirable.

7 Conclusions

This work validates the use of mini-C(T) specimens from four RPV steels in their unirradiated and irradiated conditions for Master Curve testing and confirms the detrimental effects of impurity elements like Cu and P. It additionally suggests improvements for the optimization of the Master Curve testing and analysis. Our findings are summarized as follows:

- JRQ and ANP-6 exhibit a higher shift in T_0 due to the presence of impurity elements such as P, Cu and Ni. The testing orientation of the samples did not significantly influence the T_0 apart from that of ANP-6. This could be due to inhomogeneities associated with the weld material.
- The T_0 obtained from mini-C(T) specimens agrees with the T_0 obtained from standard Charpy-sized specimens confirming the successful use of mini-C(T) specimens.
- Fractography indicates no significant change in location of fracture initiators on irradiation. A significant effect is however, observed for side-grooved samples.
- The highest increase in ductile fracture mode from unirradiated to irradiated state was observed for ANP-6. This aligns with its lower irradiation induced hardening and a higher loss in yield strength at high temperatures as compared to JRQ. This however, contradicts a large ΔT_0 exhibited by ANP-6. Caution must therefore be taken while interpreting the embrittlement of a material with the ductile fracture mode observed on fracture surfaces alone.
- We established an empirical correlation between test temperature and censoring probability using censoring statistics from a large number of mini-C(T) test data. Based on this, we propose a concept for the optimum choice of test temperature within a Master Curve analysis.
- The $K_{\mathrm{Jc\Delta a}}$ censoring criterion does not influence the T_0 significantly. Hence, we suggest a simplification of ASTM E1921 for the Master Curve analysis.

Acknowledgements

We acknowledge the financial support of this research by the German BMUV project "Kleinproben" (FKZ 1501592B). The authors express their gratitude to W. Webersinke, M. Roßner, V. Reinke, J. Pietzsch and T. Welz for their valuable technical support. The support of S. Mohr from the project management organisation (GRS) is also gratefully acknowledged.

References

1. Odette, G.R.; Lucas, G.E. Recent Progress in Understanding Reactor Pressure Vessel Steel Embrittlement. *Radiat. Eff. Defects Solids* **1998**, *144*, 189–231, doi:10.1080/10420159808229676.
2. Miller, M.K.; Nanstad, R.K.; Sokolov, M.A.; Russell, K.F. The Effects of Irradiation, Annealing and Reirradiation on RPV Steels. *J. Nucl. Mater.* **2006**, *351*, 216–222, doi:10.1016/j.jnucmat.2006.02.010.
3. Wallin, K. The Scatter in KIC-Results. *Eng. Fract. Mech.* **1984**, *19*, 1085–1093, doi:10.1016/0013-7944(84)90153-X.
4. Wallin, K. The Size Effect in KIC Results. *Eng. Fract. Mech.* **1985**, *22*, 149–163, doi:10.1016/0013-7944(85)90167-5.
5. Wallin, K. Irradiation Damage Effects on the Fracture Toughness Transition Curve Shape for Reactor Pressure Vessel Steels. *Int. J. Press. Vessels Pip.* **1993**, *55*, 61–79, doi:10.1016/0308-0161(93)90047-W.
6. Chaouadi, R.; Scibetta, M.; Van Walle, E.; Gerard, R. On the Use of the Master Curve Based on the Precracked Charpy Specimen. *ASME Press. Vessel Pip. Symp.* **1999**, *393*, 35–46.
7. Nanstad, R.K.; McCabe, D.E.; Sokolov, M.A.; Merkle, J.G. Experimental Evaluation of Deformation and Constraint Characteristics in Precracked Charpy and Other Three-Point Bend Specimens.; American Society of Mechanical Engineers Digital Collection, August 20 2009; pp. 259–267.
8. Chaouadi, R.; van Walle, E.; Scibetta, M.; Gérard, R. On the Use of Miniaturized CT Specimens for Fracture Toughness Characterization of RPV Materials.; American Society of Mechanical Engineers Digital Collection, December 1 2016.
9. Zurbuchen, C.; Viehrig, H.-W.; Weiss, F.-P. Master Curve and Unified Curve Applicability to Highly Neutron Irradiated Western Type Reactor Pressure Vessel Steels. *Nucl. Eng. Des.* **2009**, *239*, 1246–1253, doi:10.1016/j.nucengdes.2009.03.008.
10. Viehrig, H.-W.; Scibetta, M.; Wallin, K. Application of Advanced Master Curve Approaches on WWER-440 Reactor Pressure Vessel Steels. *Int. J. Press. Vessels Pip.* **2006**, *83*, 584–592, doi:10.1016/j.ijpvp.2006.04.005.
11. van Walle, E.; Scibetta, M.; Valo, M.J.; Viehrig, H.-W.; Richter, H.; Atkins, T.; Wootton, M.R.; Keim, E.; Debarberis, L.; Horsten, M. Reconstitution Techniques Qualification and Evaluation to Study Ageing Phenomena of Nuclear Pressure Vessel Materials (RESQUE). *Nucl. Eng. Des.* **2001**, *209*, 67–77, doi:10.1016/S0029-5493(01)00389-2.
12. Scibetta, M.; Lucon, E.; Chaouadi, R.; Walle, E. van; Gérard, R. Use of Broken Charpy V-Notch Specimens from a Surveillance Program for Fracture Toughness Determination. *J. ASTM Int.* **2005**, *3*, 1–7, doi:10.1520/JAI12450.
13. Yamamoto, M. The Master Curve Fracture Toughness Evaluation of Irradiated Plate Material JRQ Using Miniature-C(T) Specimens. In Proceedings of the PVP2017; Volume 1A: Codes and Standards, October 26 2017.

14. Miura, N.; Soneda, N. Evaluation of Fracture Toughness by Master Curve Approach Using Miniature C(T) Specimens. *J. Press. Vessel Technol.* **2012**, *134*, doi:10.1115/1.4005390.
15. Yamamoto, M. Trial Study of the Master Curve Fracture Toughness Evaluation by Mini-C(T) Specimens for Low Upper Shelf Weld Metal Linde-80.; American Society of Mechanical Engineers Digital Collection, October 26 2018.
16. Sokolov, M.A. Use of Mini-CT Specimens for Fracture Toughness Characterization of Low Upper-Shelf Linde 80 Weld Before and After Irradiation.; American Society of Mechanical Engineers Digital Collection, October 26 2018.
17. Yamamoto, M.; Carter, R.; Viehrig, H.-W.; Lambrecht, M. A Round Robin Program of MasterCurve Evaluation Using Miniature C(T) Specimens (Comparison of T0 for a Weld Metal).; IASMiRT: BEXCO, Busan, Korea, August 20 2017; p. 10.
18. Yamamoto, M.; Kimura, A.; Onizawa, K.; Yoshimoto, K.; Ogawa, T.; Mabuchi, Y.; Viehrig, H.-W.; Miura, N.; Soneda, N. A Round Robin Program of Master Curve Evaluation Using Miniature C(T) Specimens: 3rd Report — Comparison of T0 Under Various Selections of Temperature Conditions.; American Society of Mechanical Engineers Digital Collection, November 18 2014.
19. Wallin, K.; Yamamoto, M.; Ehrnstén, U. Location of Initiation Sites in Fracture Toughness Testing Specimens: The Effect of Size and Side Grooves. In Proceedings of the PVP2016; Volume 1B: Codes and Standards, July 17 2016.
20. Yamamoto, M.; Miura, N. Applicability of Miniature C(T) Specimens for the Master Curve Evaluation of RPV Weld Metal. In Proceedings of the PVP2015; Volume 1A: Codes and Standards, July 19 2015.
21. Sugihara, T.; Hirota, T.; Sakamoto, H.; Yoshimoto, K.; Tsutsumi, K.; Murakami, T. Applicability of Miniature C(T) Specimen to Fracture Toughness Evaluation for the Irradiated Japanese Reactor Pressure Vessel Steel.; American Society of Mechanical Engineers Digital Collection, October 26 2017.
22. Miller, M.K.; Nanstad, R.K.; Sokolov, M.A.; Russell, K.F. The Effects of Irradiation, Annealing and Reirradiation on RPV Steels. *J. Nucl. Mater.* **2006**, *351*, 216–222, doi:10.1016/j.jnucmat.2006.02.010.
23. Altstadt, E.; Keim, E.; Hein, H.; Serrano, M.; Bergner, F.; Viehrig, H.-W.; Ballesteros, A.; Chaouadi, R.; Wilford, K. FP7 Project LONGLIFE: Overview of Results and Implications. *Nucl. Eng. Des.* **2014**, *278*, 753–757, doi:10.1016/j.nucengdes.2014.09.003.
24. Viehrig, H.-W.; Altstadt, E.; Houska, M.; Valo, M. Fracture Mechanics Characterisation of the Beltline Welding Seam of the Decommissioned WWER-440 Reactor Pressure Vessel of Nuclear Power Plant Greifswald Unit 4. *Int. J. Press. Vessels Pip.* **2012**, *89*, 129–136, doi:10.1016/j.ijpvp.2011.10.016.
25. Ando, K.; Mogami, K.; Tuji, K. Probabilistic Aspects of Cleavage Crack Initiation Sites and Fracture Toughness. *Fatigue Fract. Eng. Mater. Struct.* **1992**, *15*, 1171–1184, doi:10.1111/j.1460-2695.1992.tb01255.x.

26. Yang, W.-J.; Lee, B.-S.; Oh, Y.-J.; Huh, M.-Y.; Hong, J.-H. Microstructural Parameters Governing Cleavage Fracture Behaviors in the Ductile–Brittle Transition Region in Reactor Pressure Vessel Steels. *Mater. Sci. Eng. A* **2004**, *379*, 17–26, doi:10.1016/j.msea.2003.10.289.
27. Tanguy, B.; Besson, J.; Piques, R.; Pineau, A. Ductile to Brittle Transition of an A508 Steel Characterized by Charpy Impact Test: Part I: Experimental Results. *Eng. Fract. Mech.* **2005**, *72*, 49–72, doi:10.1016/j.engfracmech.2004.03.010.
28. E08 Committee *Test Method for Determination of Reference Temperature, To, for Ferritic Steels in the Transition Range ASTM E1921-2021*; ASTM International;
29. INTERNATIONAL ATOMIC ENERGY AGENCY Reference Manual on the IAEA JRQ Correlation Monitor Steel for Irradiation Damage Studies. *IAEA* **2001**, *Report number IAEA-TECDOC-1230*.
30. Viehrig, H.-W.; Zurbuchen, C. Application of the Master Curve Regarding Characterization of the Toughness of Neutron Irradiated Reactor Pressure Vessel Steels. *HZDR* **2007**, *Internal report FZD-476 2007*.
31. Ulbricht, A.; Hein, H.; Hernandez-Mayoral, M.; Onorbe, E.; Etienne, A.; Meslin, E.; Brumovsky, M. The Effect of Neutron Flux on Irradiation Induced Damage of RPV Steels. *SOTERIA* **2018**, *Report D2.1*.
32. Ritter, S.; Seifert, H.P. *Characterisation of the Lower Shell and Weld Material of the Biblis C Reactor Pressure Vessel*; PSI Bericht Nr. 02-01; Paul Scherrer Institut: CH – 5232 Villigen PSI, 2002;
33. Serrano, M.; Lydman, J.; Hurley, C.; Karlsen, W.; Kobiela, J.; Hein, H.; Neukam, M.; Radiguet, B.; Bergner, F.; Viehrig, H.-W.; et al. Microstructural Inhomogeneities of RPV Steels and Their Impact On Mechanical Properties at Initial State. *SOTERIA* **2017**, *Report D3.1*.
34. Viehrig, H.-W.; Ulbricht, A.; Bergner, F.; Hein, H.; Radiguet, B.; Lydman, J.; Karlsen, W.; Brumovsky, M.; Hernandez-Mayoral, M. Effects of Initial Materials Inhomogeneities on Microstructure and Mechanical Properties of RPV Steels at Irradiated State for LTO. *SOTERIA* **2019**, *Report D3.2*.
35. Scibetta, M.; Lucon, E.; van Walle, E. Optimum Use of Broken Charpy Specimens from Surveillance Programs for the Application of the Master Curve Approach. *Int. J. Fract.* **2002**, *116*, 231–244, doi:10.1023/A:1020165900918.
36. Altstadt, E.; Bergner, F.; Houska, M. Use of the Small Punch Test for the Estimation of Ductile-to-Brittle Transition Temperature Shift of Irradiated Steels. *Nucl. Mater. Energy* **2021**, *26*, 100918, doi:10.1016/j.nme.2021.100918.
37. Hein, H.; Barthelmes, J.; Gillemot, F.; Serrano, M.; Hernandez-Mayoral Documentation and Data of Materials for Microstrucural Analysis. *LONGLIFE* **2012**, *Report D3.1 revision 2*.
38. Reaktorsicherheitskommission RSK-Guidelines for PWR Reactors. *RSK-Leitlinien Fuer Druckwasserreaktoren* **1979**.

39. J. D. Landes J Calculation - Front Face Displacement Measurement on a Compact Specimen. *Int. J. Fract.* **1980**, *16*.

40. Das, A.; Chekhonin, P.; Houska, M.; Obermeier, F.; Altstadt, E. Master Curve Testing of RPV Steels Using Mini-C(T) Specimens – Irradiation Effects and Censoring Statistics. *Nucl. Mater. Energy* **2023**, *34*, 101395, doi:10.1016/j.nme.2023.101395.

41. Yamamoto, M.; Ukai, S.; Hayashi, S.; Kaito, T.; Ohtsuka, S. Reverse Phase Transformation from α to γ in 9Cr-ODS Ferritic Steels. *J. Nucl. Mater.* **2011**, *417*, 237–240, doi:10.1016/j.jnucmat.2010.12.250.

42. Bhattacharya, A.; Zinkle, S.J.; Henry, J.; Levine, S.M.; Edmondson, P.D.; Gilbert, M.R.; Tanigawa, H.; Kessel, C.E. Irradiation Damage Concurrent Challenges with RAFM and ODS Steels for Fusion Reactor First-Wall/Blanket: A Review. *J. Phys. Energy* **2022**, *4*, 034003, doi:10.1088/2515-7655/ac6f7f.

43. U.S. Nucl. Regulatory Commission Radiation Embrittlement of Nuclear Reactor Vessel Materials, Regulatory Guide 1.99, Revision 2. **1988**.

44. Ericksonkirk, M.; Ericksonkirk, M. The Relationship between the Transition and Upper-Shelf Fracture Toughness of Ferritic Steels. *Fatigue Fract. Eng. Mater. Struct.* **2006**, *29*, 672–684, doi:10.1111/j.1460-2695.2006.01026.x.

45. EricksonKirk, M.; EricksonKirk, M. An Upper-Shelf Fracture Toughness Master Curve for Ferritic Steels. *Int. J. Press. Vessels Pip.* **2006**, *83*, 571–583, doi:10.1016/j.ijpvp.2006.05.001.

46. T. L. Anderson *Fracture Meechanics - Fundamentals and Applications*; Third.; Taylor & Francis: Boca Raton, Florida, USA, 2005; ISBN 0-8493-1656-1.

Appendix

A 1 Master Curve individual test data for unirradiated JRQ

Code	Orientation	Thickness B [mm]	Initial crack length a_0 [mm]	T-T_0 [K]	Elastic Modulus [GPa]	Yield strength [MPa]	K_{JC} [MPa√m]	$K_{JC(limit)}$ [MPa√m]	Δa Censoring 0-cens 1-valid	a_0 shape 0-inv 1-val	Overall censoring 0-cens 1-valid
1	T-L	4.00	4.04	-20.1	209.86	576.54	118.87	132.56	1	1	1
2	T-L	3.99	4.01	-20.1	209.86	576.54	123.01	133.59	1	1	1
3	T-L	3.97	4.00	-30.1	209.97	594.48	74.71	135.48	1	1	1
4	T-L	3.98	4.01	-30.1	209.97	594.48	98.72	135.16	1	1	1
5	T-L	4.01	4.00	-40.1	210.09	614.72	106.19	137.40	1	1	1
6	T-L	3.98	4.04	-40.1	210.09	614.72	123.06	136.77	1	1	1
7	T-L	3.99	3.99	-40.1	210.09	614.72	57.91	137.68	1	1	1
8	T-L	4.00	4.00	-50.1	210.20	637.47	43.11	140.53	1	1	
9	T-L	3.96	3.96	-50.1	210.20	637.47	96.73	140.48	1	1	
10	T-L	3.99	3.92	-50.1	210.20	637.47	70.09	141.48	1	1	
11	T-L	3.98	4.17	-25.1	209.92	585.23	96.88	131.25	1	0	
12	T-L	3.98	4.00	-25.1	209.92	585.23	85.24	133.99	1	1	1
13	T-L	3.98	4.06	-35.1	210.03	604.30	107.95	135.26	1	1	1
14	T-L	4.01	4.02	-35.1	210.03	604.30	52.02	135.88	1	1	1
15	T-L	4.01	4.04	-45.1	210.14	625.77	102.68	138.09	1	1	1
16	T-L	4.01	3.99	-45.1	210.14	625.77	53.14	138.88	1	1	1
17	T-S	4.01	4.19	-27.2	210	594	118.88	132.61	1	1	1
18	T-S	4.00	3.94	-27.2	210	594	90.50	136.69	1	1	1
19	T-S	4.02	3.99	-37.2	210	615	145.09	138.26	1	1	0
20	T-S	4.02	4.01	-37.2	210	615	88.81	137.61	1	1	1
21	T-S	3.98	3.93	-47.2	210	637	91.27	141.53	1	1	1
22	T-S	4.00	3.94	-47.2	210	637	84.53	141.64	1	1	1
23	T-S	3.96	3.93	-27.2	210	594	200.82	138.10	0	1	0
24	T-S	4.00	3.97	-32.2	210	604	99.12	137.26	1	1	1
25	T-S	3.98	3.79	-32.2	210	604	85.77	139.94	1	1	1
26	T-S	3.99	3.90	-32.2	210	604	56.97	138.38	1	1	1
27	T-S	3.97	3.95	-37.2	210	615	97.09	138.72	1	1	1
28	T-S	4.00	4.03	-37.2	210	615	75.68	137.22	1	1	1
29	T-S	4.00	3.88	-27.2	210	594	85.45	137.38	1	1	1
30	T-S	3.97	3.95	-22.2	210	585	56.28	135.29	1	1	1
31	T-S	4.02	3.91	-22.2	210	585	41.74	135.84	1	1	1
32	T-S	3.96	3.92	-22.2	210	585	80.86	135.91	1	1	1

A 2 Master Curve individual test data for irradiated JRQ

Code	Orientation	Thickness B [mm]	Initial crack length a_0 [mm]	T-T_0 [K]	Elastic Modulus [GPa]	Yield strength [MPa]	K_{JC} [MPa√m]	$K_{JC(limit)}$ [MPa√m]	Δa Censoring 0-cens 1-valid	a_0 shape 0-inv 1-val	Overall censoring 0-cens 1-valid
0	T-L	3.97	3.97	-9.5	207	801	129.17	157.85	1	1	1
1	T-L	3.98	3.98	-34.5	207	808	49.18	159.96	1	0	
2	T-L	4.01	4.01	-34.5	207	808	107.04	153.94	1	1	1
3	T-L	4.00	4.00	-24.5	207	805	83.51	155.90	1	1	1
4	T-L	3.96	3.96	-24.5	207	805	102.36	155.56	1	1	1
5	T-L	4.00	4.00	-24.5	207	805	105.92	155.63	1	1	1
6	T-L	4.00	4.00	-19.5	207	804	98.17	157.78	1	1	1
7	T-L	3.98	3.98	-14.5	207	803	92.07	157.30	1	1	1
9	T-L	4.00	4.00	-14.5	207	803	101.04	153.67	1	1	1
A	T-L	3.96	3.96	-19.5	207	804	81.26	157.36	1	1	1
B	T-L	3.99	3.99	-19.5	207	804	156.23	157.51	1	1	1
C	T-L	3.98	3.98	-29.5	207	807	102.66	154.55	1	1	1
D	T-L	3.97	3.97	-29.5	207	807	98.01	156.51	1	1	1
E	T-L	4.02	4.02	-39.5	208	809	100.10	156.91	1	1	1
F	T-L	3.94	3.94	-39.5	208	809	125.64	159.33	1	1	1

A 3 Master Curve individual test data for unirradiated JFL

Code	Orientation	Thickness B [mm]	Initial crack length a_0 [mm]	T-T_0 [K]	Elastic Modulus [GPa]	Yield strength [MPa]	K_{JC} [MPa√m]	$K_{JC(limit)}$ [MPa√m]	Δa Censoring 0-cens 1-valid	a_0 shape 0-inv 1-val	Overall censoring 0-cens 1-valid
1	L-T	3.97	4.02	-23.4	210	607	110.82	136.09	1	1	1
2	L-T	3.98	3.99	-23.4	210	607	119.17	137.03	1	1	1
3	L-T	3.99	4.12	-23.4	210	607	75.34	134.59	1	1	1
4	L-T	3.99	4.10	-13.4	210	591	155.87	132.69	1	1	0
5	L-T	3.99	4.14	-33.4	210	625	58.08	136.51	1	1	1
6	L-T	4.00	4.01	-33.4	210	625	114.02	138.97	1	1	1
7	L-T	3.99	4.04	-33.4	210	625	84.66	137.97	1	1	1
8	L-T	4.00	4.03	-40.4	211	638	133.26	139.74	1	1	1
9	L-T	4.00	3.93	-40.4	211	638	79.42	141.34	1	1	1
10	L-T	3.99	4.03	-40.4	211	638	70.98	140.01	1	1	1
11	L-T	3.98	4.12	-23.4	210	607	127.31	135.11	1	1	1
12	L-T	4.00	4.00	-33.4	210	625	74.12	138.93	1	1	1
13	L-T	4.00	4.03	-40.4	211	638	102.45	139.72	1	1	1
14	L-T	4.00	3.95	-23.4	210	607	96.56	137.42	1	1	1
15	L-T	3.98	3.96	-33.4	210	625	64.98	139.33	1	1	1
16	L-T	3.98	3.99	-40.4	211	638	38.04	140.51	1	1	1
17	T-S	4.00	3.98	-30.8	210	607	51.31	137.39	1	1	1
18	T-S	3.99	3.97	-30.8	210	607	93.32	137.42	1	1	1
19	T-S	4.00	4.08	-30.8	210	607	136.26	135.34	1	1	0
20	T-S	4.00	4.15	-40.8	210	625	83.21	135.95	1	1	1
21	T-S	4.01	4.02	-40.8	210	625	96.84	138.50	1	1	1
22	T-S	4.00	3.98	-40.8	210	625	91.33	139.09	1	1	1
23	T-S	3.98	4.04	-47.8	211	638	53.14	139.61	1	1	1
24	T-S	3.99	4.00	-47.8	211	638	64.18	140.48	1	1	1
25	T-S	3.99	3.98	-47.8	211	638	53.74	140.86	1	1	1
26	T-S	4.00	4.08	-35.8	210	616	104.36	136.72	1	1	1
27	T-S	3.99	4.01	-35.8	210	616	100.41	137.40	1	1	1
28	T-S	3.99	4.05	-43.8	210	631	49.07	138.88	1	1	1
29	T-S	4.00	3.97	-43.8	210	631	55.48	140.40	1	1	1
30	T-S	3.99	4.06	-43.8	210	631	85.80	138.41	1	1	1
31	T-S	4.00	3.97	-37.8	210	620	61.58	138.99	1	1	1
32	T-S	3.98	3.96	-37.8	210	620	81.48	138.85	1	1	1
33	T-S	4.01	4.02	-33.8	210	613	82.27	137.50	1	1	1
34	T-S	4.00	3.98	-33.8	210	613	84.89	138.01	1	1	1
35	T-S	4.01	3.96	-45.8	210	634	69.14	141.11	1	1	1
36	T-S	4.01	3.98	-45.8	210	634	38.22	140.71	1	1	1
37	T-S	4.03	4.06	-25.8	210	599	190.80	134.74	1	1	0
38	T-S	4.02	3.97	-25.8	210	599	109.28	135.56	1	1	1
39	T-S	4.02	3.87	-25.8	210	599	123.10	137.65	1	1	1
40	T-S	4.01	3.92	-30.8	210	607	92.85	137.73	1	1	1
41	T-S	4.01	4.01	-35.8	210	616	164.92	137.37	1	1	0

A 4 Master Curve individual test data for irradiated JFL

Code	Orientation	Thickness B [mm]	Initial crack length a_0 [mm]	T-T_0 [K]	Elastic Modulus [GPa]	Yield strength [MPa]	K_{JC} [MPa√m]	$K_{JC(limit)}$ [MPa√m]	Δa Censoring 0-cens 1-valid	a_0 shape 0-inv 1-val	Overall censoring 0-cens 1-valid
0	L-T	3.98	3.84	-12.9	210	689	85.86	147.18	1	1	1
1	L-T	3.94	3.84	-12.9	210	689	87.57	146.10	1	1	1
2	L-T	3.97	3.87	-2.9	209	679	212.92	144.71	0	1	0
3	L-T	3.97	3.83	-2.9	209	679	114.80	145.37	1	1	1
4	L-T	3.96	3.98	2.1	209	675	283.59	144.16	0	1	0
5	L-T	3.97	3.96	-7.9	210	684	125.38	143.01	1	1	1
6	L-T	3.94	3.87	-7.9	210	684	217.59	146.16	0	1	0
7	L-T	3.94	3.75	-17.9	210	694	104.15	148.48	1	1	1
8	L-T	3.96	4.07	-17.9	210	694	117.99	144.19		1	1
9	L-T	3.97	4.01	-22.9	210	699	66.13	145.42	1	1	1
A	L-T	3.95	3.89	-22.9	210	699	118.37	147.45	1	1	1
B	L-T	3.99	3.89	-12.9	210	689	49.26	146.49	1	1	1
C	L-T	3.94	4.02	-17.9	210	694	143.38	144.51	1	1	1
D	L-T	3.99	3.83	-22.9	210	699	168.20	147.99	1	1	0
E	L-T	3.97	3.92	-27.9	210	705	77.29	147.52	1	1	1
F	L-T	3.95	3.83	-27.9	210	705	115.56	147.84	1	1	1
G	T-S	4.03	3.91	-22.5	210	699	68.95	147.81	1	1	1
H	T-S	4.01	4.03	-17.5	210	694	87.90	143.35	1	1	1
I	T-S	3.92	4.11	-7.5	210	684	229.60	143.64	0	1	0
J	T-S	3.95	4.05	-22.5	210	699	71.62	145.64	1	1	1
K	T-S	3.95	3.99	-17.5	210	694	118.89	144.95	1	1	1
L	T-S	4.02	4.04	-22.5	210	699	123.21	144.80	1	1	1
M	T-S	3.98	3.64	-27.5	210	705	121.81	152.69	1	1	1
N	T-S	3.94	4.03	-22.5	210	699	83.38	144.65	1	1	1
O	T-S	3.97	3.90	-17.5	210	694	179.53	146.21	1	1	0
P	T-S	4.01	3.71	-27.5	210	705	240.34	151.01	0	1	0
Q	T-S	3.92	3.83	-12.5	210	689	117.30	147.28	1	1	1
R	T-S	3.84	3.98	-17.5	210	694	116.88	145.23	1	1	1
S	T-S	4.01	3.92	-22.5	210	699	60.70	146.59	1	1	1
T	T-S	3.95	4.02	-7.5	210	684	234.01	142.73	0	1	0
U	T-S	3.95	4.05	-2.5	209	679	124.87	143.79	1	1	1
V	T-S	3.95	3.90	-27.5	210	705	194.23	148.51	1	1	0
W	T-S	4.03	3.91	-32.5	210	711	46.95	149.58	1	1	1
X	T-S	4.00	3.92	-32.5	210	711	54.07	148.25	1	1	1
Y	T-S	3.97	3.97	-27.5	210	705	66.64	147.16	1	1	1
Z	T-S	4.01	3.86	-12.5	210	689	82.26	147.48	1	1	1

A 5 Master Curve individual test data for ANP-3 in the T-L orientation

Code	Irradiation state	Thickness B [mm]	Initial crack length a_0 [mm]	T-T_0 [K]	Elastic Modulus [GPa]	Yield strength [MPa]	K_{JC} [MPaVm]	$K_{JC(limit)}$ [MPaVm]	Δa Censoring 0-cens 1-valid	a_0 shape 0-inv 1-val	Overall censoring 0-cens 1-valid
1	Unirr	4.00	3.95	-21.2	215	548	120.80	132.00	1	1	1
2	Unirr	4.01	3.86	-21.2	215	548	64.73	133.48	1	1	1
3	Unirr	4.03	3.93	-11.2	214	534	106.39	130.59	1	1	1
4	Unirr	4.03	3.91	-11.2	214	534	183.69	130.97	1	1	0
5	Unirr	4.02	3.88	-16.2	215	541	163.71	132.21	1	1	0
6	Unirr	4.02	3.88	-16.2	215	541	254.71	133.07	1	1	0
7	Unirr	3.99	3.83	-26.2	215	555	96.91	134.54	1	1	1
8	Unirr	4.00	4.04	-26.2	215	555	224.54	131.01	1	1	0
9	Unirr	4.02	4.01	-31.2	216	562	109.99	133.13	1	1	1
10	Unirr	4.02	3.92	-31.2	216	562	57.09	134.64	1	1	1
11	Unirr	4.02	3.96	-36.2	216	569	82.92	134.56	1	1	1
12	Unirr	4.03	4.05	-36.2	216	569	71.38	133.44	1	1	1
13	Unirr	4.00	4.03	-36.2	216	569	90.88	134.02	1	1	1
14	Unirr	4.01	4.05	-26.2	215	555	124.62	131.68	1	1	0
15	Unirr	4.01	4.07	-16.2	215	541	121.72	128.97	1	1	1
16	Unirr	4.03	3.88	-31.2	216	562	86.86	134.87	1	1	1
0	Irr	3.99	3.85	-11.2	211	645	166.79	143.13	1	1	0
1	Irr	3.94	4.09	-21.2	212	654	117.58	140.99	1	1	1
2	Irr	3.99	4.05	-21.2	212	654	104.35	141.96	1	1	1
3	Irr	3.92	4.04	-6.2	211	641	134.58	138.72	1	1	1
4	Irr	4.00	3.93	-6.2	211	641	115.49	141.36	1	1	1
5	Irr	3.96	4.02	-1.2	210	637	184.18	139.64	1	1	0
6	Irr	3.98	4.01	-1.2	210	637	164.67	138.92	1	1	0
7	Irr	3.96	3.93	-26.2	212	659	55.37	143.69	1	1	1
8	Irr	3.97	3.99	-11.2	211	645	131.97	140.88	1	1	1
9	Irr	3.89	3.84	-11.2	211	645	94.03	143.49	1	1	1
A	Irr	3.94	3.90	-11.2	211	645	107.78	142.66	1	1	1
B	Irr	3.95	3.93	-21.2	212	654	105.18	143.15	1	1	1
C	Irr	3.97	3.92	-21.2	212	654	176.35	143.47	1	0	0
D	Irr	3.98	3.80	-16.2	211	650	92.62	144.32	1	1	1
E	Irr	3.99	3.88	-16.2	211	650	118.70	143.00	1	1	1
F	Irr	3.92	4.04	-16.2	211	650	160.17	140.48	1	1	0

A 6 Master Curve individual test data for unirradiated ANP-6

Code	Orientation	Thickness B [mm]	Initial crack length a_0 [mm]	T-T_0 [K]	Elastic Modulus [GPa]	Yield strength [MPa]	K_{JC} [MPa√m]	$K_{JC(limit)}$ [MPa√m]	Δa Censoring 0-cens 1-valid	a_0 shape 0-inv 1-val	Overall censoring 0-cens 1-valid
1	T-L	4.02	4.06	-5.3	213	648	101.34	141.34	1	1	1
2	T-L	4.01	4.05	-5.3	213	648	224.77	141.38	0	1	0
3	T-L	4.02	4.05	-5.3	213	648	125.65	141.55	1	1	1
4	T-L	4.02	4.05	-15.3	214	660	143.03	141.92	1	1	0
5	T-L	4.02	4.05	-25.3	214	672	74.29	144.38	1	1	1
6	T-L	4.00	4.02	-25.3	214	672	41.57	144.88	1	1	1
7	T-L	3.98	4.02	-15.3	214	660	146.36	143.84	1	1	0
8	T-L	3.95	4.04	-25.3	214	672	90.81	144.52	1	1	1
9	T-L	3.98	3.97	-25.3	214	672	98.53	145.61	1	1	1
10	T-L	3.95	4.03	-15.3	214	660	146.70	142.96	1	1	0
11	T-L	3.58	3.98	-15.3	214	660	59.23	144.11	1	1	1
29	T-S	4.02	3.79	6.0	214	660	331.78	148.07	0	1	0
30	T-S	4.03	4.08	-14.0	215	684	271.25	145.90	0	1	0
31	T-S	4.01	4.06	-28.0	216	703	138.90	148.58	1	1	1
32	T-S	4.01	4.06	-29.0	216	705	113.35	148.80	1	1	1
33	T-S	4.02	4.05	-29.0	216	705	65.56	149.10	1	1	1
34	T-S	4.04	4.15	-19.0	215	691	78.90	145.42	1	1	1
35	T-S	4.03	4.07	-19.0	215	691	93.23	147.18	1	1	1
36	T-S	4.03	4.08	-19.0	215	691	72.01	146.80	1	1	1
37	T-S	4.01	4.06	-19.0	215	691	81.36	146.97	1	1	1
38	T-S	4.03	4.08	-14.0	215	684	127.36	145.72	1	1	1
39	T-S	4.01	4.03	-14.0	215	684	73.67	146.72	1	1	1
40	T-S	4.02	4.06	-14.0	215	684	199.21	146.33	0	1	0

A 7 Master Curve individual test data for irradiated ANP-6

Code	Orientation	Thickness B [mm]	Initial crack length a_0 [mm]	T-T_0 [K]	Elastic Modulus [GPa]	Yield strength [MPa]	K_{JC} [MPa√m]	$K_{JC(limit)}$ [MPa√m]	Δa Censoring 0-cens 1-valid	a_0 shape 0-inv 1-val	Overall censoring 0-cens 1-valid
0	T-S	3.98	3.96	-11.5	203	787	138.90	153.86	1	1	1
1	T-S	4.02	3.86	8.5	202	780	133.03	155.06	0	1	0
2	T-S	3.93	4.02	-1.5	202	784	160.70	152.30	0	1	0
3	T-S	4.02	4.09	-11.5	203	787	95.13	151.07	1	1	1
4	T-S	3.94	3.90	-11.5	203	787	100.98	154.70	1	1	1
5	T-S	4.01	4.00	-21.5	204	791	80.50	153.61	1	1	1
7	T-S	3.97	4.08	-1.5	202	784	108.79	150.48	1	1	1
8	T-S	3.50	4.04	-6.5	203	785	169.31	151.73	0	1	0
9	T-S	4.00	4.08	-21.5	204	791	129.57	151.37	0	1	0
A	T-S	3.93	4.11	-21.5	204	791	138.49	151.90	0	1	0
B	T-S	3.99	4.23	-21.5	204	791	131.56	150.18	0	1	0
C	T-S	3.98	3.76	-21.5	204	791	53.64	157.87	1	1	1
D	T-S	4.00	3.62	-11.5	203	787	77.81	159.44	1	1	1
E	T-S	3.99	3.91	-16.5	203	789	60.55	154.65	1	1	1
F	T-S	4.00	3.97	-16.5	203	789	105.68	154.11	1	1	1

HELMHOLTZ ZENTRUM
DRESDEN ROSSENDORF

Bautzner Landstr. 400
01328 Dresden, Germany
Phone +49 351 260-2276
Fax +49 351 260-12276
Email e.altstadt@hzdr.de
http://www.hzdr.de